Energy Engineering

Tech Science Press

https://doi.org/10.32604/ee.2026.080617

ARTICLE

Enhanced Adaptive Super-Twisting Current-Constrained Control of PMSM Based on Generalized Proportional-Integral Observer

Boqiang Wei* and **Yiwei Feng**

College of Automation and Electrical Engineering, Lanzhou University of Technology, Lanzhou, China

*Corresponding Author: Boqiang Wei. Email: weibq@lut.edu.cn

Received: 13 February 2026; Accepted: 15 April 2026; Published: 30 August 2026

ABSTRACT: This paper presents an advanced control strategy, termed enhanced adaptive super-twisting current-constrained algorithm (CCEASTA), to address overcurrent protection challenges and reject disturbances in non-cascade permanent magnet synchronous motors (PMSM) drives. The proposed strategy consists of two fundamental components. Firstly, a gain-adaptive super-twisting sliding mode controller with current constraints is designed in a non-cascade framework. The purpose of this structure is to suppress chattering, accelerate dynamic response, and ensure overcurrent protection. Secondly, a generalized proportional-integral observer (GPIO) is incorporated to estimate unknown state variables and external disturbances in real time. The estimates thus obtained facilitate feed-forward compensation, thereby significantly reducing the impact of disturbances on the system.

KEYWORDS: Permanent magnet synchronous motor; current-constrained control; enhanced adaptive super-twisting algorithm; generalized proportional-integral observer

1 Introduction

The permanent magnet synchronous motor (PMSM) has been found to be a highly effective solution for servo systems, owing to its high power density, excellent dynamic performance, and control flexibility [1]. Conventionally, the control of PMSM speed is implemented via a cascade structure consisting of an outer speed loop and an inner current loop. This configuration, historically constrained by hardware limitations, operated the two loops at different rates, resulting in a sequential delay. Such a configuration often complicates parameter tuning and limits the dynamic response. In light of contemporary advancements in computational resources, the execution of both the current and speed loops can be conducted in parallel. This configuration facilitates a non-cascade control architecture, which, in turn, simplifies system design and enhances performance.

The non-cascade structure has been shown to simplify design and reduce the number of adjustable parameters in comparison with its cascade counterpart, thus rendering it a prominent research focus. For instance, reference [2] presents a control method that integrates generalized predictive control with a nonlinear disturbance observer within this non-cascade framework. This approach is designed to enhance the dynamic performance of PMSM systems and streamline parameter tuning. Meanwhile, reference [3] investigates a dual three-phase PMSM system subject to time-varying disturbances and adopts a non-cascade hierarchical control architecture to streamline controller design. Furthermore, reference [4] proposes a fast non-singular terminal sliding-mode speed control strategy under a similar non-cascade structure to overcome the adaptability limitations of conventional PI controllers.

However, in the non-cascade structure, the merging of the current and speed loops changes the q-axis current from an output to a state variable. Consequently, conventional PID controllers are no longer capable of effectively constraining it, which may result in damaging transient overcurrents. Whilst the selection of more conservative (lower-gain) parameters has the potential to mitigate the risk of overcurrent, it is inevitable that this will result in the degradation of the system's dynamic performance. In order to address transient overcurrent in non-cascade PMSM drives, a range of state-constrained control strategies have been proposed [5]. For instance, Reference [6] proposed a reference trajectory modulation method for nonlinear systems with unknown parameters, which enforces constraints by using the reference signal as a closed-loop input. Nevertheless, ensuring constraints over an infinite horizon remains practically challenging due to overly restrictive requirements on the reference signal class. Alternatively, the invariant set method guarantees that states remain within prescribed limits and can address both input saturation and state constraints [7]. Nevertheless, the computational intricacy inherent in ascertaining the invariant set frequently restricts its applicability to particular initial conditions. Another common approach is model predictive control (MPC), which has been shown to handle constraints by design [8]. Despite its extensive utilisation, MPC necessitates a precise model, exhibits sensitivity to disturbances, and demands considerable computational resources, thereby impeding its practical implementation. To summarise the aforementioned analysis, the following conditions must be satisfied to resolve the overcurrent issue under non-cascade PMSM control: The primary objective is to constrain the current within a limited range. The second objective is to construct an easily implementable control system. The third objective is to ensure that the dynamic steady state performance is satisfactory. In this paper, novel constrained controllers are designed with two objectives in mind. Firstly, these controllers are intended to avoid overly complex constraints, such as the reference track line modulation method. Secondly, they are designed to avoid limiting the initial values, for example, using an invariant set, or requiring an exact system model, for example, using MPC.

In order to address the current constraint in non-cascade PMSM drives, this paper proposes a controller that incorporates a current-limiting penalty mechanism into the adaptive gain design. Specifically, a penalty function is constructed based on the current limit, which approaches infinity as the q-axis current nears the boundary, thereby effectively suppressing transient overcurrent. However, traditional PI control is deficient in terms of robustness against parameter variations and external disturbances. Among the various robust control alternatives, Sliding-mode control (SMC) has been extensively adopted in motor drives, robotics, aerospace, and power electronics due to its robust stability, rapid response, and structural simplicity. However, the practical implementation of SMC is constrained by factors such as finite control bandwidth and discrete sampling, which induce high-frequency chattering. This chattering has the potential to induce substantial torque ripple, thereby compromising system stability. Consequently, the suppression of chattering is imperative for enhancing the steady-state performance of SMC systems [9,10].

In order to mitigate the impact of chattering vibration in the sliding mode control, literature [11] proposes the adoption of fuzzy switching gain adjustment, a methodology that eliminates the interference term through the effective estimation of the switching gain. However, this approach can compromise the robustness of the control system. Literature [12] proposes a finite-time sliding mode control, which aims to suppress the chattering effect associated with conventional SMC within a finite period of time. However, the method requires high mathematical accuracy and is difficult to apply to practical systems. Literature [13] adopts a second-order super-twisting algorithm (STA), which ensures the strong robustness of the system while eliminating the chattering vibration, and thus has become a research hotspot in PMSM control. As described in [14], a fast super-twisting non-singular fast terminal sliding mode controller has been developed. This controller has been shown to attenuate system singularity and chattering phenomenon, improve the switching convergence rate, and exhibit a faster convergence rate in comparison to traditional second-order sliding modes. Literature [15] proposes a novel generalized adaptive super-twisting algorithm for the accurate estimation of the control gain, with the concomitant suppression of chattering vibration and the prevention of redundant signal transmission. Literature [16] proposes the use of an enhanced adaptive super-twisting sliding mode observer, a technique that has been demonstrated to reduce the discontinuity of the control system, reduce the inherent chattering vibration, and effectively suppress the torque fluctuation. However, the method does not take into account the effect of disturbance on the system control performance.

The permanent magnet synchronous motor control system is affected by a variety of disturbance factors, including harmonic disturbance caused by unstable power supply voltage, torque fluctuation generated by sudden change of load torque, parameter variations triggered by temperature change and magnetic saturation, as well as systematic disturbance caused by delays in signal acquisition and measurement error, etc. The combined effect of these disturbances on the dynamic and steady-state performance of the system is a primary factor in the necessity to enhance the system's performance in the disturbance rejection capacity. These disturbances jointly affect the dynamic and steady state performance of the control system, rendering the disturbance rejection problem a key challenge to improving the system's performance. Therefore, this paper proposes to utilize a generalized proportional-integral observer (GPIO), which is developed based on linear observer theory. In comparison with the conventional frequency-domain disturbance observer, the generalized proportional-integral observer (GPIO) has the capacity to be applied to a range of disturbance types and can estimate the system's internal states, external disturbances and their derivatives of each order in real time. In comparison with the traditional time-domain disturbance observer, the structure of the GPIO is relatively simple and can balance the dynamic response of the system and its noise suppression performance, making it more applicable in practice [17,18].

The paper proposes an enhanced adaptive controller, termed CCEASTA (enhanced adaptive super-twisting current-constrained algorithm), which integrates current constraint with an improved super-twisting sliding-mode algorithm within a non-cascade structure, building upon the foundation of reference [19]. The paper proposes a fourth-order generalized proportional-integral observer (GPIO) to accurately estimate the total collective disturbance and facilitate feed-forward compensation, thus improving the disturbance rejection performance of the permanent magnet synchronous motor (PMSM) speed control system. This composite controller, which combines the CCEASTA and GPIO, effectively limits the q-axis current of the PMSM to a manageable range, thereby safeguarding the hardware from overcurrent while maintaining the system's dynamic performance [20]. Furthermore, the adaptive super-twisting sliding mode control employs a continuously differentiable switching function and speed-adaptive gain, thereby significantly reducing chattering and enhancing adaptability across the full-speed domain. The construction of the GPIO facilitates the estimation of disturbances and their higher-order derivatives, thereby enhancing both dynamic and steady-state performance, as well as disturbance resistance. This paper also incorporates practical non-ideal factors into the simulations, including sensor noise, discretization delay, inverter non-linearity, and voltage saturation, to assess the feasibility and robustness of the proposed strategy within an engineering implementation context. This approach offers a safe and practical solution for high-performance permanent magnet synchronous motor drives.

2 PMSM Mathematical Model

It can be posited that, under the condition that the magnetic field is sinusoidally distributed, and with the assumption that hysteresis and eddy current losses are negligible, and further that the magnetic circuit is not saturated [21], the mathematical model of the surface-mounted permanent-magnet synchronous motor in the dq-rotating coordinate system can be expressed as follows:

$$\begin{pmatrix} \dot{i}_d \\ \dot{i}_q \\ \dot{\omega}_m \end{pmatrix} = \begin{pmatrix} -\frac{R_s}{L_s} & n_p\omega_m & 0 \\ -n_p\omega_m & -\frac{R_s}{L_s} & -\frac{n_p\psi_f}{L_s} \\ 0 & \frac{n_p\psi_f}{J} & -\frac{B}{J} \end{pmatrix} \begin{pmatrix} i_d \\ i_q \\ \omega_m \end{pmatrix} + \begin{pmatrix} \frac{u_d}{L_s} \\ \frac{u_q}{L_s} \\ -\frac{T_L}{J} \end{pmatrix} \tag{1}$$

where i_d and i_q are the stator currents in the d-axis and q-axis, respectively, and u_d and u_q are the stator voltages in the d-axis and q-axis, respectively, noting that n_p is the number of pole pairs, ω_m is the mechanical angular velocity, R_s is the stator resistance, L_s is the inductance, T_L is the load torque, ψ_f is the rotor magnetic chain, B is the coefficient of viscous friction, and J is the inertia of rotation.

The system equation of motion can be expressed as:

$$J\frac{d\omega_m}{dt} = T_e - T_L - B\omega_m \tag{2}$$

where T_e is the electromagnetic torque.

The system electromagnetic torque equation can be expressed as:

$$T_e = \frac{3}{2}n_p\psi_f i_q = K, i_q \tag{3}$$

where K_t is set to be the torque constant.

When establishing the mathematical model of the permanent magnet synchronous motor speed control system, in order to more accurately reflect the actual operating conditions, it is necessary to take into account the internal parameters of the control system as well as the time-varying influence of the external load torque. Therefore, its rotor motion equation should be constructed and described on this basis as:

$$\frac{d\omega_m}{dt} = -\left(\frac{B}{J} + \Delta a\right)\omega_m - \left(\frac{T_L}{J} + \Delta c\right) + \left(\frac{n_p\psi_f}{J} - \Delta b\right) i_{q_0} = a\omega_m + bu - d \tag{4}$$

In the system modeling, $a = -\frac{B}{J}, b = \frac{n_p\psi_f}{J}, u = i_q$ represents the designed control input law, Δa, Δb, Δc are used to characterize the parameter variations generated by the motor during actual operation, and d integrates the aggregate disturbance [22] triggered by the above parameter changes in conjunction with external load torque fluctuations. thus, the following relation can be obtained:

$$d = \Delta a\omega_m + \Delta bu + \Delta c + \frac{T_z}{J} \tag{5}$$

Current constraints are introduced to limit the q-axis stator current to $|i_\mathrm{q}|$.

Assumption 1: *The system load torque variation satisfies the following conditions:*

$$\frac{2T_L + B\omega_m^*}{n_p\psi_f} < c_{\mathrm{or}}T_L < n_p\psi_f\left(c - i_q^*\right) \tag{6}$$

where $i_q^* = \frac{T_z + B\omega_m^*}{n_p\psi_f}$ *is set as the current balance point.*

Remark 2.1: *If the load meets the conditions of Assumption 1 in the unknown case, the current constraint still has a margin to suppress the load change, so* $c - i^\star_q > 0$ *must be valid. c value is generally determined according to the rated current of the PMSM, which is usually two to three times of the rated current, and in this paper,* $c = 15A$*.*

3 Enhanced Adaptive Super-Twisting Sliding Mode Current Constrained Controller Design

3.1 Current Constraint Function Design

In this paper, the barrier function is designed so that the constraint boundaries can be adjusted according to the state of the system while guaranteeing $\left|i_q\right| < c$:

$$\Phi\left(i_q\right) = \begin{cases} \frac{c^2}{2}\ln\left(\frac{c^2}{c^2 - i_q^2}\right) + \frac{1}{2}i_q^2, & \left|i_q\right| < c \\ \infty, & \left|i_q\right| \geq c \end{cases} \tag{7}$$

Deriving the above equation yields the penalty term

$$\phi\left(i_q\right) = \frac{\partial\Phi}{\partial i_q} = \frac{2c^2 - i_q^2}{c^2 - i_q^2} i_q \tag{8}$$

Property 3.1: *When condition $\left|i_q\right| \to c^-$ is satisfied, result $\phi\left(i_q\right) \to \pm\infty$ can be achieved and the current constraint function will form an infinity value.*

Property 3.2: *Condition $\Phi\left(i_q\right) \geq \frac{1}{2}i_q^2$ satisfies the positive characterization.*

Property 3.3: *$\phi\left(i_q\right)$ is continuously differentiable in the interval $(-c, c)$.*

To avoid singularities in the numerical calculations, a small constant $\varepsilon > 0$ is introduced in the penalty term:

$$\tilde{\Phi}\left(i_q\right) = \frac{c^2 + \epsilon}{2}\ln\left(\frac{c^2 + \varepsilon}{c^2 + \varepsilon - i_q^2}\right) + \frac{1}{2}i_q^2 \tag{9}$$

Remark 3.1: *As the q axis current i_q approaches the constraint boundary c both the barrier function $\Phi\left(i_q\right)$ and its derivative $\phi\left(i_q\right)$ exhibit a rapid increase in numerical stiffness and saturation of the control variable. To mitigate this issue, a small constant ε is introduced into the penalty term (refer to Eq. (9)) to restrict the maximum amplitude $\phi\left(i_q\right)$ and prevent calculation overflow. In the actual simulation, ε is set to 0.001. At this value, $\phi\left(i_q\right)$ at $i_q = 14.999$ A is approximately 10^3, and the corresponding control increment remains within the voltage limit range, with a maximum voltage increment of about 5 V. If ε is excessively small (for instance, $\varepsilon < 1 \times 10^{-5}$), $\phi\left(i_q\right)$ can exceed 10^5 near the boundary, potentially leading to high-frequency chattering of the control variable and numerical overflow. Conversely, if ε is too large (for example, $\varepsilon > 0.1$), the penalty effect near the boundary diminishes, resulting in a reduced constraint effect. The ε value chosen in this study strikes a balance between the strictness of constraints and numerical stability. Furthermore, the existing constraint term $\lambda_2\phi\left(i_q\right)$ is incorporated into the control law (15). As i_q approaches c, this term becomes predominant in the control variable, compelling i_q to decrease and thereby naturally preventing continuous control saturation. The simulation did not exhibit any numerical divergence or control saturation issues attributable to the barrier function.*

3.2 Enhanced Adaptive Super-Twisting Sliding Mode Control Law Design

Define the integral sliding mode surface:

$$s = e_\omega + \lambda_1\int_0^t e_\omega\left(\tau\right)d\tau + \lambda_2\Phi\left(i_q\right) \tag{10}$$

where $e_\omega = \omega_m^* - \omega_m$ is the velocity tracking error and $\lambda_1, \lambda_2 > 0$ is a design parameter.

A continuously differentiable segmented switching function is used:

$$f_\alpha(x) = \begin{cases} sign(x)\left(1 - e^{-\frac{x}{\alpha}}\right), |x| \geq \sigma \\ \frac{x}{\alpha}\left(1 - \frac{|x|}{2\alpha} + \frac{x^2}{6\alpha^2}\right), |x| < \sigma \end{cases} \tag{11}$$

where $\alpha > 0, \delta = \alpha/2$.

Property 3.4: $f_\alpha(x)$ *is second-order differentiable at* $x = 0$.

Property 3.5: $|f_\alpha(x)| \leq 1, |f_{\alpha'}(x)| \leq 1/\alpha$.

Property 3.6: $xf_\alpha(x) \geq 0$, *which guarantees positive characterization*.

Design time-varying gain

$$\begin{cases} k_1(t) = l_1\omega_e(t) + \gamma_1\|e(t)\| + \mu_1 \\ k_2(t) = l_2\omega_e^2(t) + \gamma_2\|\dot{e}(t)\| + \mu_2 \end{cases} \tag{12}$$

where $\omega_e = \max(\omega_{\min}, |\omega_m|)$, $e = \left[e_\omega, i_q\right]^T$, $\mu_1, \mu_2 > 0$ are lower bound constants.

Gaining adaptive laws:

$$\begin{cases} \dot{l}_1 = \eta_1(|s| - \epsilon_1 \, l_1) \\ \dot{l}_1 = \eta_1(|s| - \epsilon_2 \, l_2) \end{cases} \tag{13}$$

$\eta_1, \eta_2 > 0$ is the learning rate and $\epsilon_1, \epsilon_2 > 0$ is the forgetting factor.

3.3 Control Law Design

d-axis control law design:

Setting $i_d = 0$, realized with PI control:

$$u_d = k_{Pd}(0 - i_d) + k_{Id}\int_0^t (0 - i_d(\tau))\, d\tau + \omega_e L_s i_q \tag{14}$$

q-axis control law design:

$$\begin{aligned} u_q = u_{q,sq} + u_{q,z\omega} + u_{q,con} = \left(R_z i_q + \omega_s L_z i_\delta + \omega_s \psi_f + L_z i_q^{ref}\right) \\ - L_z\left[k_1|s|^{1/2} f_\alpha(s) + \int_0^t k_2 f_\alpha(s)\, d\tau\right] - \lambda_2\phi\left(i_q\right) \end{aligned} \tag{15}$$

where $\omega_e = n_p\omega_m, \dot{i}_q^{ref} = \frac{J}{K_t}\left(\dot{\omega} m^* + \lambda_1 e\omega\right) + \frac{B}{K_t}\omega_m + \frac{T_L}{K_t}$.

4 Generalized Proportional Integral Observer Design

4.1 Disturbance Modeling and Observer Structure

Modeling of aggregate disturbances:

Define the set total disturbance $d(t)$ in conjunction with the control system:

$$d(t) = -\frac{K_t}{J}\left(i_q^{ref} - i_q\right) - \frac{T_L}{J} - \frac{B}{J}\omega_m + \Delta(t) \tag{16}$$

Let $d(t)$ be expressed as a second order polynomial:

$$d\left(t\right)=a_0+a_1t+a_2t^2 \tag{17}$$

Remark 4.1: *Eq. (17) approximates the lumped disturbance d(t) using a second-order polynomial model. This approach effectively captures slowly varying disturbances, such as gradual changes in load torque, ramp disturbances, including acceleration variations, and certain low-frequency harmonic disturbances, such as the sixth harmonic induced by the inverter dead zone, which are commonly observed in actual PMSM systems. Although this model may not accurately capture high-frequency random perturbations, such as measurement noise, or non-polynomial disturbances like step or square waves, the GPIO can still provide reliable estimations owing to its high-gain observer structure. The configuration of the observer poles effectively balances estimation accuracy and sensitivity to noise.*

Extended state space model:

Defining the extended state vector $\mathbf{x}=\left[x_1,x_2,x_3,x_4\right]^T=\left[\omega_m,d,\dot{d},\ddot{d}\right]^T$, the dynamic equations of the system can be expressed as:

$$\begin{cases}\dot{x}_1=\frac{K_t}{J}i_q+x_2\\ \dot{x}_2=x_3\\ \dot{x}_3=x_4\\ \dot{x}_4=d^{(3)}\left(t\right)\end{cases} \tag{18}$$

Fourth-order GPIO design:

The design of the fourth-order generalized proportional-integral observer can be expressed as:

$$\begin{cases}\dot{z}_1=\frac{K_t}{J}i_q+z_2+\beta_1\left(\omega_m-z_1\right)\\ \dot{z}_2=z_3+\beta_2\left(\omega_m-z_1\right)\\ \dot{z}_3=z_4+\beta_3\left(\omega_m-z_1\right)\\ \dot{z}_4=\beta_4\left(\omega_m-z_1\right)\end{cases} \tag{19}$$

where z_1 is the rotational speed estimate, z_2 is the disturbance estimate, z_3 is the first order derivative of the disturbance estimate, and z_4 is the second order derivative of the disturbance estimate.

4.2 Parameter Integral and Stability Analysis

Generalized proportional-integral observer pole configuration design:

Set the observer error dynamic equation as:

$$\dot{\mathbf{e}}=A_ce+Bd^{(3)}\left(t\right) \tag{20}$$

where $\mathrm{e}=\left[e_1,e_2,e_3,e_4\right]^T=\left[\omega_m-z_1,d-z_2,\dot{d}-z_3,\ddot{d}-z_4\right]^T$, $A_c=\begin{bmatrix}-\beta_1&1&0&0\\-\beta_2&0&1&0\\-\beta_3&0&0&1\\-\beta_4&0&0&0\end{bmatrix}$.

The characteristic polynomial corresponding to the set error dynamic equation is:

$$\det\left(sI-A_e\right)=s^4+\beta_1s^3+\beta_2s^2+\beta_3s+\beta_4 \tag{21}$$

To obtain the desired dynamic response, the observer poles are configured as $-\omega_0$ (quadruple poles), i.e., the desired characteristic polynomial is:

$$(s+\omega_0)^4 = s^4 + 4\omega_0 s^3 + 6\omega_0^2 s^2 + 4\omega_0^3 s + \omega_0^4$$

Comparison of the coefficients gives: $\beta_1 = 4\omega_0, \beta_2 = 6\omega_0^2, \beta_3 = 4\omega_0^3, \beta_4 = \omega_0^4$.

Optimal selection of observer bandwidth:

The observer bandwidth parameter ω_0 selection requires a balance between dynamic response speed and noise rejection capability:

Construct the noise transfer function:

$$G_n(s) = \frac{z_1}{\sigma_n} = \frac{4\omega_0 s^3 + 6\omega_0^2 s^2 + 4\omega_0^3 s + \omega_0^4}{(s+\omega_0)^4} \tag{22}$$

Construct the disturbance suppression transfer function:

$$G_d(s) = \frac{z_1}{\delta_i} = \frac{s^3}{(s+\omega_0)^4} \tag{23}$$

All things considered, $\omega_0 = 30$ rad/s was chosen to correspond:

$$\beta_1 = 120, \beta_2 = 5400, \beta_3 = 108{,}000, \beta_4 = 810{,}000$$

Proof of stability:

Theorem 4.1: *For an observer error system, the estimation error is eventually bounded if $d^{(3)}(t)$ is bounded and $\omega_0 > 0$.*

Proof: construct the Lyapunov function $V_e = \mathbf{e}^T P \mathbf{e}$, where P satisfies $A_e^T P + P A_e = -Q$. The derivation is obtained:

$$\dot{V}_e = -e^T Q e + 2e^T P B d^{(3)}(t) \tag{24}$$

is given by $\left|d^{(3)}(t)\right| \le \overline{d}_3$:

$$\dot{V} \le -\lambda_{\min}(Q)\,\|e\|^2 + 2\,\|P\|\,\|B\|\,\left\|\overline{d}_3\right\|\,\|e\| \tag{25}$$

When $|\mathbf{e}| > \frac{2|P||\mathrm{B}|\overline{d}3}{\lambda\min(Q)}$, $\dot{V}_e < 0$,the error is therefore bounded. The proof is complete. □

Feedforward compensation design:

The feed-forward compensated control volume is designed based on the disturbance estimates provided by the generalized proportional-integral observer:

$$u_{ff} = -\frac{J}{K_t} z_2 \tag{26}$$

This feedforward term can be combined with the system control law to realize active suppression of disturbances and improve the overall robustness of the system.

5 Composite Control System Design

In order to simultaneously achieve accurate disturbance estimation and strict current limiting control, a composite control scheme is designed in this paper. The core of the scheme lies in the combination of enhanced adaptive super-twisting current constraint control (for direct current constraint) and generalized proportional-integral observer (for feed-forward compensation), and its overall control law consists of the following components:

$$\begin{aligned} u_q = u_{q,eq} + u_{q,sw} + u_{q,con} + u_{ff} = \left(R_s i_q + \omega_e L_s i_d + \omega_e \psi_f + L_s \dot{i}_q^{ref} \right) \\ - L_s \left[\mathrm{k}_1 |s|^{1/2} f\alpha\left(\mathrm{s}\right) + \int_0^t \mathrm{k}_2 f_\alpha\left(s\right) \mathrm{d}\tau \right] - \lambda_2 \phi\left(i_q\right) - \frac{J}{K_t} z_2 \end{aligned} \tag{27}$$

The overall block diagram of the control system designed in this paper is shown in Fig. 1.

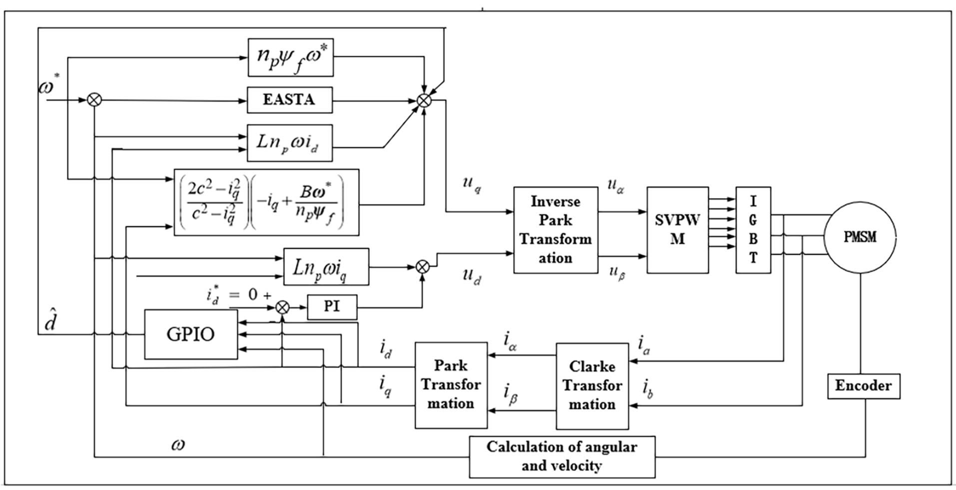

Figure 1: Block diagram of the enhanced CCEASTA system with GPIO for PMSM.

6 System Stability Analysis

6.1 Main Symbols and Assumptions

To facilitate the subsequent analysis, we first describe the main notations used in the text (as shown in Table 1) and establish the necessary theoretical assumptions.

Main Symbols:

Table 1: Definitions of key symbols.

Symbol	Description
s	Sliding surface variables
e_ω	Speed tracking error
i_q	Q-axis current
c	Maximum permissible current
$\Phi(i_q)$	Current constrained barrier function
$\phi(i_q)$	Barrier function derivative

(Continued)

Table 1 (continued)

Symbol	Description
λ_1, λ_2	Sliding surface design parameters
k_1, k_2	Adaptive sliding mode gain
$f_\alpha(x)$	Enhanced switching function
α	Boundary layer thickness
ρ	System disturbance term
σ	Integral disturbance term
δ	Perturbative derivative term

Hypothesis:

To complete the proof of stability of the system, we introduce the following three basic assumptions:

Assumption 6.1 (Disturbance boundedness): *The system disturbance satisfies the following bounded conditions:*

$$\left| \rho \right| \le \Delta_1, \quad \left| \delta \right| \le \Delta_2, \quad \left| \dot{\delta} \right| \le \Delta_3 \tag{28}$$

where $\Delta_1, \Delta_2, \Delta_3 > 0$ *is a known constant.*

Assumption 6.2 (Nature of the current constraint function): *The current constraint function* $\phi\left(i_q\right)$ *is satisfied:*

Positive characterization: $\phi\left(i_q\right) i_q > 0, \forall i_q \neq 0$.

Boundedness: $0 < \phi_{\min} \le \phi\left(i_q\right) \le \phi_{\max} < \infty, \forall |i_q| < c$.

Continuity: $\phi\left(i_q\right)$ *is continuously micro-miniaturizable within* $(-c, c)$.

Boundary characteristics: $\lim_{|i_q| \to c^-} \phi\left(i_q\right) = \pm\infty$.

Assumption 6.3 (Switching function properties): *Enhanced switching function* $f_\alpha\left(x\right)$ *satisfied:*

Continuity: $f_\alpha\left(x\right)$ *is continuous on* R.

Boundedness: $|f_\alpha\left(x\right)| \le 1, \forall x \in$ R.

Positive characterization: $x f_\alpha\left(x\right) \ge 0, \forall x \in$ R.

Boundary layer properties: when $|x| < \alpha$, $f_\alpha\left(x\right) \approx \frac{x}{\alpha}$ *can be obtained.*

6.2 Derivation of Error Dynamic Equations

Define the sliding mode surface:

$$s = e_\omega + \lambda_1 \int_0^t e_\omega\left(\tau\right) d\tau + \lambda_2 \Phi\left(i_q\right) \tag{29}$$

Derivation of Eq. (29) yields the dynamic rate of change of the slip mold surface:

$$\dot{s} = \dot{e_\omega} + \lambda_1 e_\omega + \lambda_2 \phi\left(i_q\right) \dot{i_q} \tag{30}$$

Putting the q-axis voltage control law:

$$u_q = \left(R_s i_q + \omega_e L_s i_d + \omega_e \psi_f + L_s \dot{i}_q^{ref}\right) - L_s\left[k_1 |s|^{1/2} f_\alpha(s) + \int_0^t k_2 f_\alpha(s)\, d\tau\right] - \lambda_2 \phi\left(i_q\right) \tag{31}$$

Substituting into the q-axis voltage equation:

$$L_s \frac{di_q}{dt} = u_q - R_s i_q - \omega_e L_s i_d - \omega_e \psi_f \tag{32}$$

Collation leads to the dynamic equation for the q-axis current:

$$\frac{di_q}{dt} = i'' - k_1 |s|^{1/2} f_\alpha(s) - \int_0^{\prime} k_2 f_\alpha(s)\, d\tau - \frac{\lambda_2}{L_s}\phi\left(i_q\right) \tag{33}$$

Dynamic equations for a sliding mode surface

Substitute Eq. (33) into Eq. (30) and organize the equation to obtain Eq. (34):

$$\dot{s} = \rho - \lambda_2 \phi\left(i_q\right) \mathrm{k}_1 |\mathrm{s}|^{1/2} f_\alpha(\mathrm{s}) + \sigma \tag{34}$$

Among them:

$$\rho = \dot{e}_\omega + \lambda_1 e_\omega + \lambda_2 \phi\left(\mathrm{i_q}\right) \dot{\mathrm{i}}_q^{ref} - \frac{\lambda_2^2}{L_s}\phi^2\left(\mathrm{i_q}\right) \tag{35}$$

$$\sigma = -\lambda_2 \phi\left(i_q\right) \int_0^t \mathrm{k}_2 f_\alpha(\mathrm{s})\, \mathrm{d}\tau \tag{36}$$

Auxiliary variable definitions:

The derivation of σ yields:

$$\dot{\sigma} = -\lambda_2 \frac{d\phi\left(i_q\right)}{dt} \int_0^t \mathrm{k}_2 f_\alpha(\mathrm{s})\, \mathrm{d}\tau - \lambda_2 \phi\left(\mathrm{i_q}\right) \mathrm{k}_2 f_\alpha(\mathrm{s}) \tag{37}$$

Let Eq. (38) be satisfied to obtain Eq. (39)

$$\delta = -\lambda_2 \frac{d\phi\left(i_q\right)}{dt} \int_0^t \mathrm{k}_2 f_\alpha(s)\, \mathrm{d}\tau \tag{38}$$

$$\dot{\sigma} = -\lambda_2 \phi\left(i_q\right) k_2 f_\alpha(s) + \delta \tag{39}$$

6.3 Standard Super-Twisting Sliding Mode Control Law Transformation

Define state variables: $x_1 = s, x_2 = \sigma$.

Eqs. (34) and (39) can be represented as:

$$\begin{cases} \dot{x}_1 = \rho - \lambda_2 \phi\left(\mathrm{i_q}\right) \mathrm{k}_1 |x_1|^{1/2} f_\alpha(x_1) + x_2 \\ \dot{x}_2 = -\lambda_2 \phi\left(\mathrm{i_q}\right) \mathrm{k}_2 f_\alpha(x_1) + \delta \end{cases} \tag{40}$$

Disturbance boundary analysis:

It follows from Assumption 6.1 and Assumption 6.2 that there exists a normal number $\Delta_1, \Delta_2, \Delta_3$ that makes:

$$\left| \ \rho \ \right| \leq \Delta_1, \quad \left| \ \delta \ \right| \leq \Delta_1, \quad \left| \ \dot{\delta} \ \right| \leq \Delta_3 \tag{41}$$

and $\phi\left(i_q\right)$ is satisfied:

$$0 < \phi_{min} \leq \phi\left(i_q\right) \leq \phi_{max} < \infty \tag{42}$$

6.4 Lyapunov Function Construction and Detailed Analysis

Define the vector:

$$z = \begin{bmatrix} |x_1|^{1/2} sign\left(x_1\right) \\ x_2 \end{bmatrix} \tag{43}$$

where sign () is the sign function.

Lyapunov function selection:

A quadratic Lyapunov function is chosen:

$$V = z^T P z = p_{11} z_1^2 + 2 p_{12} z_1 z_2 + p_{22} z_2^2 \tag{44}$$

where P is a symmetric positive definite matrix:

$$P = \begin{bmatrix} p_{11} & p_{12} \\ p_{12} & p_{22} \end{bmatrix} > 0 \tag{45}$$

Parameterization of matrix P:

The super-twisting algorithm is set up according to its requirements for stability:

$$P = \frac{1}{2} \begin{bmatrix} 4k_2 + k_1^2 & -k_1 \\ -k_1 & 2 \end{bmatrix} \tag{46}$$

where k_1, k_2 is a positive constant. This matrix is satisfied:
1. Symmetry: $P = P^T$.
2. Positive characterization: $p_{11} > 0$ and $det\left(P\right) > 0$.

Calculating the determinant gives:

$$det\left(P\right) = \frac{1}{4}\left[\left(4k_2 + k_1^2\right) \cdot 2 - \left(-k_1\right)^2\right] = \frac{1}{4}\left(8k_2 + 2k_1^2 - k_1^2\right) = \frac{1}{4}\left(8k_2 + k_1^2\right) > 0 \tag{47}$$

6.5 Proof of Stability

Step 1: Calculate the time derivative of z.

By defining $z_1 = |x_1|^{1/2} \text{sign}\left(x_1\right)$, the derivation is obtained:

$$\dot{z}_1 = \frac{1}{2\left|x_1\right|^{1/2}} \dot{x}_1 \cdot sign\left(\mathrm{x}_1\right) = \frac{1}{2\left|x_1\right|^{1/2}} \dot{x}_1 \cdot \frac{x_1}{|x_1|} = \frac{1}{2\left|x_1\right|^{1/2}} \dot{x}_1 \tag{48}$$

where $\text{sign}\left(x_1\right) = x_1/|x_1|$.

Substituting the $\dot{x}_1$ expression yields:

$$\dot{z}_1 = \frac{1}{2\mid x_1\mid^{1/2}}\left[\rho - \lambda_2\phi\left(i_q\right)\mathrm{k}_1\mid x_1\mid^{1/2} f_\alpha\left(x_1\right) + x_2\right] \tag{49}$$

By organizing $|x_1|^{1/2} = |z_1|$ and $x_2 = z_2$, we can obtain:

$$\dot{z}_1 = -\frac{1}{2}\lambda_2\phi\left(i_q\right)\mathrm{k}_1 f_\alpha\left(x_1\right) + \frac{1}{2}z_2 + \frac{\rho}{2\mid z_1\mid} \tag{50}$$

Taking the derivative of z_2 yields:

$$\dot{z}_2 = \dot{x}_2 = -\lambda_2\phi\left(i_q\right)\mathrm{k}_2 f_\alpha\left(x_1\right) + \delta \tag{51}$$

Step 2: Matrix form representation

Write Eqs. (47) and (48) in matrix form:

$$\dot{z} = Az + B \tag{52}$$

Among them:

$$A = \begin{bmatrix} -\frac{1}{2}\lambda_2\phi\left(i_q\right)\mathrm{k}_1 & \frac{1}{2} \\ -\frac{1}{2}\lambda_2\phi\left(i_q\right)\mathrm{k}_2 & 0 \end{bmatrix} \tag{53}$$

$$B = \begin{bmatrix} \frac{\rho}{2|z_1|} \\ \delta \end{bmatrix} \tag{54}$$

Step 3: Calculate the Lyapunov function derivative

Derive for $V = \mathbf{z}^T P\mathbf{z}$:

$$\dot{V} = \dot{z}TPz + zTP\dot{z} \tag{55}$$

Substitute Eq. (52):

$$\begin{aligned} \dot{V} &= (Az + B)^T Pz + z^T P(Az + B) \\ &= z^T\left(A^T P + PA\right)z + B^T Pz + z^T PB \\ &= z^T\left(A^T P + PA\right)z + 2z^T PB \end{aligned} \tag{56}$$

Step 4: Matrix $A^T P + PA$ calculation

Calculation $A^T P + PA$:

$$A^T P = \begin{bmatrix} -\frac{1}{2}\lambda_2\phi\mathrm{k}_1 & -\lambda_2\phi\mathrm{k}_2 \\ \frac{1}{2} & 0 \end{bmatrix}\begin{bmatrix} p_{11} & p_{12} \\ p_{12} & p_{22} \end{bmatrix} = \begin{bmatrix} -\frac{1}{2}\lambda_2\phi\mathrm{k}_1 p_{11} - \lambda_2\phi\mathrm{k}_2 p_{12} & -\frac{1}{2}\lambda_2\phi\mathrm{k}_1 p_{12} - \lambda_2\phi\mathrm{k}_2 p_{22} \\ \frac{1}{2}p_{11} & \frac{1}{2}p_{12} \end{bmatrix} \tag{57}$$

$$PA = \begin{bmatrix} p_{11} & p_{12} \\ p_{12} & p_{22} \end{bmatrix}\begin{bmatrix} -\frac{1}{2}\lambda_2\phi\mathrm{k}_1 & \frac{1}{2} \\ -\lambda_2\phi\mathrm{k}_2 & 0 \end{bmatrix} = \begin{bmatrix} -\frac{1}{2}\lambda_2\phi\mathrm{k}_1 p_{11} - \lambda_2\phi\mathrm{k}_1 p_{12} & \frac{1}{2}p_{11} \\ -\frac{1}{2}\lambda_2\phi\mathrm{k}_1 p_{12} - \lambda_2\phi\mathrm{k}_2 p_{22} & \frac{1}{2}p_{12} \end{bmatrix} \tag{58}$$

The two equations are added together to obtain:

$$A^T P + PA = \begin{bmatrix} -\lambda_2\phi \mathrm{k}_1 p_{11} - 2\lambda_2\phi \mathrm{k}_2 p_{12} & 0 \\ 0 & \frac{1}{2}p_{12} \end{bmatrix} \tag{59}$$

Step 5: Disturbance term analysis

The disturbance term $2\mathbf{z}^T PB$ can be expressed as:

$$2z^T PB = 2\begin{bmatrix} z_1 & z_2 \end{bmatrix} \begin{bmatrix} p_{11} & p_{12} \\ p_{12} & p_{22} \end{bmatrix} \begin{bmatrix} \frac{\rho}{2|z_1|} \\ \delta \end{bmatrix} \tag{60}$$

Eq. (60) is calculated as Eq. (61):

$$2z^T PB = (\mathrm{p}_{11} z_1 + \mathrm{p}_{12} z_2)\frac{\rho}{|z_1|} + 2(\mathrm{p}_{12} z_1 + \mathrm{p}_{22} z_2)\delta \tag{61}$$

By the Cauchy-Schwartz inequality:

$$\left|(p_{11} z_1 + p_{12} z_2)\frac{\rho}{|z_1|}\right| \le (\mathrm{p}_{11}|z_1| + |p_{12}||z_2|)\frac{\Delta_1}{|z_1|} = p_{11}\Delta_1 + |p_{12}|\Delta_1\frac{|z_2|}{|z_1|} \tag{62}$$

$$|2(p_{12} z_1 + p_{22} z_2)\delta| \le 2(|p_{12}||z_1| + p_{22}|z_2|)\Delta_2 \tag{63}$$

Step 6: Finite time convergence conditions

To guarantee $\dot{V} < 0$, the following conditions need to be satisfied:

Condition 6.1 (Main diagonal dominance condition):

$$-\lambda_2\phi_{\min}\mathrm{k}_1 p_{11} - 2\lambda_2\phi_{\min}\mathrm{k}_2 p_{12} + \frac{1}{2}p_{12} < 0 \tag{64}$$

Condition 6.2 (Disturbance suppression condition): *There exists* $\epsilon > 0$ *such that* Eq. (65) *holds.*

$$\begin{aligned} &-\left[\lambda_2\phi_{min}\mathrm{k}_1 p_{11} + 2\lambda_2\phi_{min}\mathrm{k}_2 p_{12} - \frac{1}{2}p_{12}\right] \| z \|^2 \\ &\quad + p_{11}\Delta_1 + |p_{12}|\Delta_1\frac{|z_2|}{|z_1|} + 2(|p_{12}||z_1| + p_{22}|z_2|)\Delta_2 \le -\epsilon \|z\|^2 \end{aligned} \tag{65}$$

Step 7: Gain selection strategy

From the conditions Eqs. (57) and (58), the gain selection strategy is derived:

The lower bound of k_1 is as in Eq. (66):

$$\mathrm{k}_1 > \frac{|p_{12}|}{2\lambda_2\phi_{\min} p_{11}} + \frac{2\mathrm{k}_2 p_{12}}{p_{11}} \tag{66}$$

The upper bound of k_2 is as in Eq. (67):

$$\mathrm{k}_2 > \frac{p_{12}}{4\lambda_2\phi_{\min} p_{12}} = \frac{1}{4\lambda_2\phi_{\min}} \tag{67}$$

The following conditions need to be met in order to suppress the disturbance:

$$\mathrm{k}_1 > \frac{2\Delta_1}{\lambda_2\phi_{\min}} \quad , \quad \mathrm{k}_2 > \frac{\Delta_2}{\lambda_2\phi_{\min}} \tag{68}$$

The gain condition can be obtained as:

$$\begin{cases} \mathrm{k}_1 > \max\left(\frac{|p_{12}|}{2\lambda_2\phi_{\min}p_{11}} + \frac{2\mathrm{k}_2 p_{12}}{p_{11}}, \frac{2\Delta_1}{\lambda_2\phi_{\min}}\right) \\ \mathrm{k}_2 > \max\left(\frac{1}{4\lambda_2\phi_{\min}}, \frac{\Delta_2}{\lambda_2\phi_{\min}}\right) \end{cases} \tag{69}$$

Step 8: Finite time convergence proof

Theorem 6.1 (Finite time convergence): *If the gains* k_1, k_2 *satisfy the condition Eq. (69) and there exists a constant* $\gamma > 0, \beta \in (0,1)$, *such that Eq. (70) holds:*

$$\dot{V} \le -\gamma V^{\beta} \tag{70}$$

Then the state of the system converges to the slip mold surface $T \le \frac{V^{1-\beta}(0)}{\gamma(1-\beta)}$ in finite time $s = 0$.

Remark 6.1: *Theorem 6.1 ensures that the system state converges to the sliding surface defined by* $s = 0$ *within a finite time frame. Based on the classical convergence analysis of the super-twisting algorithm [16], the convergence time* T *adheres to the following upper bound estimation condition:*

$$T \le \frac{2V^{1/2}(0)}{\varepsilon} \tag{71}$$

where $V(0)$ *represents the initial value of the Lyapunov function, and* A *is a constant associated with the gain. Based on the gain condition outlined in Eq. (62) and the derivative of the Lyapunov function presented in Eq. (64), we can derive*

$$\varepsilon = 2\sqrt{\lambda_{\min}(P)}\left(k_1 - \frac{\rho^+}{2}\right) \tag{72}$$

By appropriately increasing k_1 *and* k_2, *it is possible to reduce the convergence time; however, one must consider the amplitude limit of the control input and the stability margin of the system. In practical parameter selection,* ε *can initially be estimated based on the desired convergence speed, after which the lower bound of the required gain can be derived from Eq. (62).*

Proof: From Eqs. (51), (52) and (55), there exist positive constants α_1, α_2 such that Eq. (69) holds when condition (71) is satisfied.

$$\dot{V} \le -\alpha_1 \parallel z \parallel^2 + \alpha_2 \parallel z \parallel \tag{73}$$

Since $V = \mathbf{z}^T P\mathbf{z}$, there exists a constant $\kappa_1, \kappa_2 > 0$ satisfying Eq. (72)

$$\kappa_1 \parallel z \parallel 2 \le V \le \kappa_2 \parallel z \parallel^2 \tag{74}$$

Substituting Eq. (73) into Eq. (72) yields:

$$\dot{V} \le -\frac{\alpha_1}{\kappa_2}V + \frac{\alpha_2}{\sqrt{\kappa_1}}V^{1/2} \tag{75}$$

When condition $V^{1/2} > \frac{\alpha_2\kappa_2}{\alpha_1\sqrt{\kappa_1}}$ is satisfied, one obtains:

$$\dot{V} \leq -\frac{\alpha_1}{2\kappa_2}V \tag{76}$$

This indicates exponential convergence of V. When V is small, the dominant term is the $V^{1/2}$ term and the system converges in finite time by the theory of finite time stability. The proof is complete. □

6.6 *Current Constraint Function Validation Analysis*

Construct the current constrained Lyapunov function:

$$V_c = \frac{1}{2}\ln\left(\frac{c^2}{c^2 - i_q^2}\right) \tag{77}$$

Constructor properties are satisfied:

1. Positive characterization: $V_c \geq 0$, and $V_c = 0 \Leftrightarrow i_q = 0$.
2. Boundary characteristics: $\lim_{t_q| \to c^-} V_c = +\infty$

Derive for V_c:

$$\dot{V}_c = \frac{i_q \dot{i}_q}{c^2 - i_q^2} \tag{78}$$

Substituting into Eq. (33) for i_q yields:

$$\begin{aligned}\dot{V}_c &= \frac{i_q}{c^2 - i_q^2}\left[\dot{i}_q^{ref} - \mathrm{k}_1|s|^{1/2}f_\alpha(s) - \int_0^t \mathrm{k}_2 f_\alpha(s)\,d\tau - \frac{\lambda_2}{L_s}\phi(i_q)\right] \\ &= \frac{i_q\dot{i}_q^{ref}}{c^2 - i_q^2} - \frac{i_q\mathrm{k}_1|s|^{1/2}f_\alpha(s)}{c^2 - i_q^2} - \frac{i_q\int_0^t f_\alpha(s)\,d\tau}{c^2 - i_q^2} - \frac{\lambda_2}{L_s}\cdot\frac{i_q\phi(i_q)}{c^2 - i_q^2}\end{aligned} \tag{79}$$

Considering the last term of Eq. (77) yields Eq. (78):

$$\frac{i_q\phi(i_q)}{c^2 - i_q^2} = \frac{i_q}{c^2 - i_q^2}\cdot\frac{2c^2 - i_q^2}{c^2 - i_q^2}i_q = \frac{(2c^2 - i_q^2)\,i_q^2}{(c^2 - i_q^2)^2} \tag{80}$$

When $|i_q| \to c^-$: When condition $|i_q| \to c^-$ is satisfied, Eq. (80) is obtained:

$$\lim_{|i_q| \to c^-}\frac{(2c^2 - i_q^2)\,i_q^2}{(c^2 - i_q^2)^2} = +\infty \tag{81}$$

Proof of Current Binding Guarantee:

Theorem 6.2 (Current constraint guarantee): *If the initial condition ssatisfy $|i_q(0)| < c$ and $\lambda_2 > 0$, the control system ensures that $|i_q(t)| < c$ holds for all $t \geq 0$.*

Proof: Construct Eq. (77) as:

$$\dot{V}_c = T_1 + T_2 + T_3 + T_4 \tag{82}$$

Among them:

$$T_1 = \frac{i_q \dot{i}_q^{ref}}{c^2 - i_q^2}$$

$$T_2 = -\frac{i_q \mathrm{k}_1 |s|^{1/2} f_\alpha(s)}{c^2 - i_q^2}$$

$$T_3 = -\frac{i_q \int_0^t \mathrm{k}_2 f_\alpha(s)\, d\tau}{c^2 - i_q^2}$$

$$T_4 = -\frac{\lambda_2}{L_s} \cdot \frac{\left(2c^2 - i_q^2\right) i_q^2}{\left(c^2 - i_q^2\right)^2} \tag{83}$$

T_4 dominates as $|i_q|$ approaches c. Let $|i_q| = c - \epsilon$, where $\epsilon > 0$ is a very small number, then Eq. (83) holds.

$$T_4 \approx -\frac{\lambda_2}{L_s} \cdot \frac{c^2}{\left(2c\,\epsilon - \epsilon^2\right)^2} \cdot (c - \epsilon)^2 \tag{84}$$

Therefore, there exists $\epsilon_0 > 0$ such that Eq. (76) holds when condition $c - |i_q| < \epsilon_0$ is satisfied.

$$\dot{V}_c < 0 \tag{85}$$

By the principle of comparison V_c does not tend to infinity, so $|i_q(t)| < c$ holds for all $t \geq 0$. This certificate completes. □

6.7 *Detailed Analysis of Adaptive Gain Stability*

Gain Error Definition

Define the ideal adaptive gain l_1^*, l_2^* and error:

$$\tilde{l}_1 = l_1 - l_1^*, \qquad \tilde{l}_2 = l_2 - l_2^* \tag{86}$$

The adaptive law Eq. (13) is constructed as:

$$\begin{cases} \dot{\tilde{l}} = \eta_1 \left(|s| - \epsilon_1\, l_1\right) \\ \dot{\tilde{l}} = \eta_2 \left(|s| - \epsilon_2\, l_2\right) \end{cases} \tag{87}$$

Construct an extended Lyapunov function:

$$V_e = V + \frac{1}{2\eta_1} \tilde{l}_1^2 + \frac{1}{2\eta_2} \tilde{l}_2^2 \tag{88}$$

Calculation of the time derivative:

Derivation of V_e yields Eq. (80).

$$\dot{V}_e = \dot{V} + \frac{1}{\eta_1} \tilde{l}_1 \dot{\tilde{l}}_1 + \frac{1}{\eta_2} \tilde{l}_2 \dot{\tilde{l}}_2 \tag{89}$$

Substituting the gain adaptive law in Eq. (81) yields:

$$\begin{aligned}\dot{V}_e &= \dot{V} + \tilde{l}_1\left(|s| - \epsilon_1\ l_1\right) + \tilde{l}_2\left(|s| - \epsilon_2\ l_2\right)\\ &= \dot{V} + |s|\left(\tilde{l}_1 + \tilde{l}_2\right) - \epsilon_1\ l_1\tilde{l}_1 - \epsilon_2\ l_2\tilde{l}_2\end{aligned} \tag{90}$$

Stability analysis:

From Eq. (74), there exists the constant $\gamma > 0$ such that:

$$\dot{V} \le -\gamma V^{1/2} \tag{91}$$

Utilizing Young's inequality:

$$|s|\left(\tilde{l}_1 + \tilde{l}_2\right) \le \frac{1}{2}s^2 + \frac{1}{2}\left(\tilde{l}_1 + \tilde{l}_2\right)^2 \le \frac{1}{2}s^2 + \tilde{l}_1^2 + \tilde{l}_2^2 \tag{92}$$

$$-\epsilon_i\ l_i\tilde{l}_i = -\epsilon_i\left(l_i^* + \tilde{l}_i\right)\tilde{l}_i = -\varepsilon_i l_i^*\tilde{l}_i - \varepsilon_i\tilde{l}_i^2 \tag{93}$$

By the Cauchy-Schwartz inequality:

$$-\epsilon_i\ l_i\tilde{l}_i \le \frac{\epsilon_i}{2}\left(l_i^{*2} + \tilde{l}_i^2\right) \tag{94}$$

Combining the two inequalities gives:

$$\dot{V}_e \le -\gamma V^{1/2} + \frac{1}{2}s^2 + \tilde{l}_1^2 + \tilde{l}_2^2 + \frac{\varepsilon_1}{2}\left(l_1^{*2} + \tilde{l}_1^2\right) - \varepsilon_1\tilde{l}_1^2 + \frac{\varepsilon_2}{2}\left(l_2^{*2} + \tilde{l}_2^2\right) - \varepsilon_2\tilde{l}_2^2 \tag{95}$$

Collating Eq. (93) yields Eq. (94):

$$\dot{V} \le -\gamma V^{1/2} + \frac{1}{2}s^2 + \frac{\epsilon_1}{2}l_1^{*2} + \frac{\epsilon_2}{2}l_2^{*2} + \left(1 + \frac{\epsilon_1}{2} - \epsilon_2\right)\tilde{l}_2^2 \tag{96}$$

When $\epsilon_1, \varepsilon_2 > 2$ is chosen, the coefficient $1 + \frac{\varepsilon_i}{2} - \varepsilon_i = 1 - \frac{\varepsilon_i}{2} < 0$, is obtained:

$$\dot{V}_e \le -\gamma V^{1/2} - \alpha_1\tilde{l}_1^2 - \alpha_2\tilde{l}_2^2 + C \tag{97}$$

where $\alpha_i = \frac{\varepsilon_i}{2} - 1 > 0$, $C = \frac{\varepsilon_1}{2}l_1^{*2} + \frac{\varepsilon_2}{2}l_2^{*2} + \frac{1}{2}s^2$ are bounded constants.

Consistent and ultimately boundedness:

Theorem 6.3 (Adaptive gain stability): *If* $\epsilon_1, \epsilon_2 > 2$, *the adaptive gain* l_1, l_2 *is consistently eventually bounded.*

Proof: From Eq. (95), when condition $\tilde{l}_i^2 > \frac{C}{\alpha_i}$ or condition $\dot{V}_e < 0$ is reached, $V^{1/2} > \frac{C}{\gamma}$ is established. By the theory of consistent eventual boundedness, there exists a tight set Ω such that all trajectories end up in and remain in Ω. The proof is complete. □

6.8 *Stability Analysis of Composite Large Signals Containing d-Axis PI with Voltage Saturation*

In Sections 6.2–6.5, the finite-time convergence of the sliding-mode dynamics was established, while Section 4.2 demonstrated the boundedness of the GPIO estimation error. However, the influence of the integral state of the *d*-axis PI controller and voltage saturation on the overall closed-loop system remains unaddressed. This section will construct a composite Lyapunov function to rigorously prove the large-signal stability of the complete interconnected system, which includes the d-axis PI controller, q-axis sliding-mode control, and GPIO.

Step 1: Extend the System State Space Definition

Based on the mathematical model of the permanent magnet synchronous motor (PMSM) (Eqs. (1)–(4)) presented in Section 2, and incorporating the d-axis proportional-integral (PI) control law alongside the q-axis sliding mode control law, the extended state vector is defined as follows:

$$\chi = [\mathrm{e}_d, \xi_d, \mathrm{s}, \sigma, \mathrm{e}_z]^T \in \mathbb{R}^6 \tag{98}$$

The definitions of each state variable are given as:

d-axis current tracking error: $e_d = i_d^{ref} - i_d$, let $i_d^{ref} = 0$, then $e_d = -i_d$.

d-axis PI integral state: ξ_d, which is designed to eliminate steady-state errors.

Sliding mode surface variable:

$$s = e_\omega + \lambda_1 \int_0^t e_\omega(\tau) d\tau$$

Auxiliary variable:

$$\sigma = \dot{s} + \lambda_2 s$$

from Eq. (35).

Observer estimation error:

$$e_z = \left[\mathrm{e}_\omega, \mathrm{e}_d, \mathrm{e}_{\dot{d}}\, \mathrm{e}_{\ddot{d}}\right]^T$$

(satisfying Eq. (20)).

d-axis current dynamics: Considering parameter perturbations and lumped disturbances on the basis of Eq. (1), the dynamic equation can be derived as:

$$\frac{di_d}{dt} = -\frac{R_s}{L_s} i_d + n_p \omega_m i_q + \frac{1}{L_s} u_d + \Delta_d \tag{99}$$

where Δ_d represents the parameter perturbations and unmodeled dynamics of the d-axis. Since $e_d = -i_\mathrm{d}$, substituting it gives the error dynamics equation of the d-axis:

$$\dot{e}_d = -\frac{R_s}{L_s} e_d - n_p \omega_m i_q - \frac{1}{L_s} u_d - \Delta_d \tag{100}$$

d-axis PI control law:

A standard PI control structure is adopted, with the control law expressed as:

$$u_d = k_{pd} e_d + k_{id} \xi_d \tag{101}$$

among them, k_{pd} and k_{id} are the PI gains. To prevent the degradation of system performance caused by integral windup, a conditional integral anti-windup strategy is applied to the integrator dynamics, and the corresponding dynamic equation is:

$$\dot{\xi}_d = \begin{cases} e_d, |\mathrm{u}_d| < \mathrm{U}_{d,\max} \quad or \quad e_d \cdot \xi_d \le 0 \\ 0, \quad other \end{cases} \tag{102}$$

where $U_{d,\max}$ is the maximum allowable value of the d-axis voltage, which is determined by the voltage saturation constraint. This strategy ensures that the integrator is frozen when the control input is saturated and the tracking error has the same sign as the integral state, thus effectively avoiding the integral windup phenomenon.

q-axis voltage control law:

The q-axis voltage control law is composed of the sliding mode control term (Eq. (15)) and the GPIO feedforward compensation term, which is expressed as:

$$u_q = u_{q0} = \frac{L_S}{K_t}\left[\dot{\omega}_m^{ref} + \lambda_2 \mathrm{e}_\omega + \mathrm{k}_1 \mathrm{f}_\alpha(\mathrm{s}) + \mathrm{k}_2 \phi\left(\mathrm{i}_q\right)\mathrm{s}\right] + \frac{R_s}{K_t} i_q + n_p \omega_m i_d - \frac{L_s}{K_t}\hat{d} \tag{103}$$

where $\hat{d}$ is the disturbance estimation value obtained by the GPIO (refer to Eq. (19)).

Voltage saturation constraint

Voltage saturation constraint: The applied voltage vector is constrained by the DC bus voltage U_{DC} of the inverter. When employing SVPWM modulation, the maximum non-distorted phase voltage amplitude is $U_{\max} = U_{DC}/\sqrt{3}$, and the saturation model is as follows:

$$u = sat\left(u_0\right) = \begin{cases} u_0, \sqrt{u_d^2 + u_q^2} \le U_{\max} \\ U_{\max}\frac{u_0}{\|u_0\|}, \sqrt{u_d^2 + u_q^2} > U_{\max} \end{cases} \tag{104}$$

Define the saturation deviation $\Delta u_{sat} = sat\left(u_0\right) - u_0$, which takes a non-zero value when the voltage saturation phenomenon occurs in the system.

Step 2: Construction of the Composite Lyapunov Function

A candidate composite Lyapunov function is constructed as the weighted sum of the Lyapunov functions corresponding to the four subsystems of the closed-loop system, and its expression is:

$$V_{total} = V_d\left(e_d, \xi_d\right) + \mathrm{V}_\omega\left(s, \sigma\right) + \mathrm{V}_{ob}\left(e_z\right) + \mathrm{V}_c\left(i_q\right) \tag{105}$$

For the d-axis PI control subsystem, a quadratic Lyapunov function containing integral states is selected, and coupling terms are introduced to optimize the convergence characteristics of the system, with the function expressed as:

$$V_d\left(e_d, \xi_d\right) = \frac{1}{2}e_d^2 + \frac{k_{id}}{2k_{pd}}\xi_d^2 + \frac{\alpha_d}{2}\left(e_d + \frac{k_{id}}{k_{pd}}\xi_d\right)^2 \tag{106}$$

where $\alpha_d > 0$ is the coupling coefficient of the Lyapunov function. The above function is positive definite, since all three terms are in the form of sum of squares and the coefficients of each term are positive real numbers.

The Lyapunov function defined for the sliding mode control subsystem in Section 6.4 (Eq. (41)) is adopted directly, with the expression:

$$V_\omega\left(\zeta\right) = \zeta^T P \zeta \;, \quad \zeta = \left[\sigma^{1/2}\mathrm{f}_\alpha\left(\mathrm{s}\right), \sigma\right]^T \tag{107}$$

where P is a symmetric positive definite matrix (Eq. (42)), which satisfies the parameterized form given in Eq. (43):

$$P = \begin{bmatrix} 2k_2 + \frac{1}{2}k_1^2 & -\frac{1}{2}k_1 \\ -\frac{1}{2}k_1 & 1 \end{bmatrix} \tag{108}$$

On the basis of the theoretical derivation in Section 4.2, the Lyapunov function for the GPIO estimation error subsystem is defined as:

$$V_{ob}\left(e_z\right) = \mathrm{e}_z^T P_{ob} e_z \tag{109}$$

where P_{ob} is a positive definite matrix, which satisfies the following Lyapunov equation:

$$A_{ob}^T P_{ob} + P_{ob} A_{ob} = -Q_{ob} \quad , \quad Q_{ob} > 0 \tag{110}$$

The barrier function defined for the current constraint subsystem in Section 6.6 (Eq. (68)) is adopted, with the expression:

$$V_c(i_q) = \frac{1}{2}\Phi\left(i_q\right) = \frac{1}{2}\cdot\frac{c^2}{c^2 - i_q^2} \tag{111}$$

This barrier function has two key properties: (i) positive definiteness in the defined domain; (ii) boundary characteristic that the function value tends to infinity when the state approaches the constraint boundary, thus ensuring that the system current always satisfies the preset constraint condition.

Step 3: Derivative Calculation of the Lyapunov Function for Each Subsystem

Derivative of the Lyapunov Function for the d-axis PI Control Subsystem

Substitute Eqs. (91) and (92) into the Lyapunov function of the d-axis PI control subsystem, and first calculate the time derivative of the function $\dot{V}_d$. The time derivative of Eq. (97) is calculated as:

$$\dot{V}_d = e_d \dot{e}_d + \frac{k_{id}}{k_{pd}} \xi_d \dot{\xi}_d + \alpha_d \left(e_d + \frac{k_{id}}{k_{pd}} \xi_d\right) \left(\dot{e}_d + \frac{k_{id}}{k_{pd}} \dot{\xi}_d\right) \tag{112}$$

In the unsaturated state of the system voltage, substitute the expressions of $\dot{e}_d$ and $\dot{\xi}_d = e_d$ into the above derivative equation, and after arrangement and simplification, the following result can be obtained:

$$\dot{V}_d = -\frac{R_s}{L_s} e_d^2 - \frac{k_{id}}{k_{pd}} \xi_d^2 - \alpha_d \left(\frac{R_s}{L_s} + \mathrm{k}_{pd}\right) \left(\mathrm{e}_d + \frac{k_{id}}{k_{pd}} \xi_d\right)^2 + \Delta_{d-cross} \tag{113}$$

where the cross-coupling term in the equation is expressed as:

$$\Delta_{d-cross} = -e_d \left(n_p \omega_m i_q + \Delta_d\right) - \alpha_d \left(e_d + \frac{k_{id}}{k_{pd}} \xi_d\right) n_p \omega_m i_q \tag{114}$$

This coupling term arises from the electromagnetic cross-coupling $-n_p \omega_m i_q$ of the motor and the parameter perturbation Δ_d. According to Assumption 6.1 and the boundedness of the rotational speed, there exist positive constants M_1 and M_2 such that:

$$\Delta_{d-cross} = -e_d \left(n_p \omega_m i_q + \Delta_d\right) - \alpha_d \left(e_d + \frac{k_{id}}{k_{pd}} \xi_d\right) n_p \omega_m i_q \tag{115}$$

Upon the occurrence of voltage saturation, an additional term $\Delta u_d = u_d - u_{d0}$ is incorporated into the derivative equation as a result of the control error. However, the conditional integral anti-windup strategy (Eq. (102)) effectively prevents the integral state of the PI controller from diverging. Furthermore, the negative definiteness of $\dot{V}_d$ is reinstated once the system exits the voltage saturation state.

From the theoretical derivation in Section 6.5, in the unsaturated state of the system voltage, the time derivative of the Lyapunov function for the sliding mode control subsystem is:

$$\dot{V}_\omega \leq -\gamma_1 V_\omega^{1/2} - \gamma_2 V_\omega + \gamma_3 \parallel \zeta \parallel \cdot \mid \Delta_{obs} \mid \tag{116}$$

where $\gamma_1, \gamma_2, \gamma_3 > 0$ is a constant related to the sliding mode control gain, and $\Delta_{obs} = d - \hat{d}$ is the estimation error of the GPIO. According to Theorem 4.1, the estimation error of the GPIO is bounded, and there exists a positive constant $\delta_{ob} > 0$ such that $\mid \Delta_{obs} \mid \leq \delta_{ob}$ holds.

According to Theorem 4.1 presented in Section 4.2, the time derivative of the Lyapunov function for the GPIO estimation error subsystem is:

$$\dot{V}_{ob} \leq -\lambda_{min}\left(Q_{ob}\right) \parallel e_z \parallel^2 + 2 \parallel P_{ob} \parallel \cdot \parallel e_z \parallel \cdot \mid \dot{d}^{(3)} \mid \tag{117}$$

where $d^{(3)}$ is the third-order time derivative of the lumped disturbance of the system, which is guaranteed to be bounded by Assumption 6.1. Therefore, there exists a positive constant $\delta_{ob} > 0$ such that $\parallel e_z \parallel \geq \delta_{ob}$, $\dot{V}_{ob} < 0$ when the system satisfies the preset conditions, which indicates that the estimation error of the GPIO is ultimately bounded.

Based on Eqs. (69)–(72) in Section 6.6, the time derivative of the barrier function (Eq. (102)) for the current constraint subsystem is calculated as:

$$\dot{V}_c = \phi\left(i_q\right) \cdot \dot{i}_q \tag{118}$$

Substitute the q-axis current dynamic equation (Eq. (32)) into the above derivative equation, and the result is:

$$V_c = \phi\left(i_q\right)\left(-\frac{R_s}{L_s} i_q + \frac{1}{L_s} u_q - n_p \omega_m i_d - \frac{1}{L_s} d\right) \tag{119}$$

Substitute the actual q-axis voltage $u_q = u_{q0} + \Delta u_q$ (where Δu_q is the voltage saturation deviation) and the q-axis voltage control law (Eq. (94)) into the above equation, and the simplified derivative equation can be obtained as:

$$\dot{V}_c = -\phi\left(i_q\right)\left[L_s R_s i_q - L_{s1}\left(u_{q0} + \Delta u_q\right) + n_p \omega_m i_d + \frac{1}{L_s} d\right] \tag{120}$$

After expanding the above equation, it can be found that $-\phi\left(i_q\right) k_2 \phi\left(i_q\right) s^2 = -k_2\left[\phi\left(i_q\right)\right]^2 s^2 \leq 0$ is the dominant term of the derivative, and all other remaining terms are bounded in the defined domain.

Step 4: Analysis of Interconnected Coupling Terms of the System

The four subsystems in the closed-loop system are coupled with each other through three main pathways, which are specifically as follows:

Electromagnetic cross-coupling: The $-n_p \omega_m i_q$ term in the d-axis error dynamic equation (Eq. (91)) and the $+n_p \omega_m i_d$ term in the q-axis current dynamic equation (Eq. (32)) form the electromagnetic cross-coupling between the d and q-axis of the PMSM.

Voltage saturation coupling: The voltage saturation constraint acts on both the d, q-axis voltages simultaneously, and u_d and u_q share the same voltage amplitude constraint, forming the coupling effect caused by voltage saturation.

Observer control coupling: The disturbance estimation value $\hat{d}$ obtained by the GPIO is applied to the feedforward compensation of the q-axis voltage control, and the estimation error of the observer will affect the dynamic characteristics of the sliding mode control subsystem, forming the control coupling based on the observer.

Define the total coupling term of the composite Lyapunov function derivative as the sum of the three coupling terms mentioned above, with its expression:

$$\Psi = \Delta_{d-cross} + \Delta_{\omega-cross} + \Delta_{sat} \tag{121}$$

where $\Delta_{\omega-cross}$ is the contribution of the electromagnetic cross-coupling term between the d, q-axis to the total coupling term, and Δ_{sat} is the contribution of the voltage saturation effect to the total coupling term.

Lemma 6.5 (Boundedness of the Total Coupling Term): *Under the premise that Assumptions 6.1–6.4 hold, there exists a positive constant C_1, C_2, C_3, C_4 such that the following inequality about the total coupling term is satisfied:*

$$|\ \Psi\ | \leq C_1 V_d^{1/2} + C_2 V_\omega^{1/2} + C_3 V_{ob}^{1/2} + C_4 \parallel \Delta u_{sat} \parallel \tag{122}$$

Proof: According to the boundedness of the motor rotational speed ($|\omega_m| \leq \omega_{\max}$) and the current constraint condition ($\left|i_q\right| < c$) of the system, it can be concluded that the variables $n_p \omega_m i_q$ and $n_p \omega_m i_d$ are bounded. Combined with the linear boundedness property shown in Eq. (106), and the variable $\Delta_{d-cross}$ can be processed by the same method, the voltage saturation deviation $\Delta_{\omega-cross}$ is also bounded. Therefore, there exists a positive constant $\parallel \Delta u_{sat} \parallel$ that satisfies the inequality in Eq. (113). □

Step 5: Derivative Estimation of the Composite Lyapunov Function

Calculate the time derivative of the composite Lyapunov function (Eq. (96)), and substitute the time derivatives of the Lyapunov functions of each subsystem obtained in Step 3 into it, with the derivative equation expressed as:

$$\dot{V}_{total} = \dot{V}_d + \dot{V}_\omega + \dot{V}_{ob} + \dot{V}_c \tag{123}$$

Substitute Eqs. (104), (107), (108) and (111) into the above equation, and combine and simplify the like terms to obtain:

$$\dot{V}_{total} \leq -\alpha_d \parallel e_d, \xi_d \parallel^2 - \gamma_1 V_\omega^{1/2} - \gamma_2 V_\omega - \lambda_{min}\left(Q_{ob}\right) \parallel e_z \parallel^2 - \beta_c V_c + \Psi \tag{124}$$

where $\beta_c > 0$ represents the leading coefficient of the current constraint term $\parallel e_d, \xi_d \parallel^2 = e_d^2 + \xi_d^2$, appropriately scaled. To address the coupling terms, we utilize the boundedness established in Lemma 6.5 and apply Young's inequality ($ab \leq \frac{1}{2}a^2 + \frac{1}{2}b^2$):

$$\Psi \leq \frac{1}{2}\alpha_d \parallel e_d, \xi_d \parallel^2 + \frac{1}{2}\gamma_1 V_\omega^{1/2} + \frac{1}{2}\lambda_{min}\left(Q_{ob}\right) \parallel e_z \parallel^2 + C \tag{125}$$

where $C = \frac{C_4^2}{2\alpha_d} + \frac{C_4^2}{2\gamma_1} + \frac{C_4^2}{2\lambda_{min}(Q_{ob})} + \frac{C_4^2}{2} \parallel \Delta u_{sat} \parallel^2$ is a positive constant related to the saturation deviation (C = 0 when saturation is not activated). Substitute Eq. (116) into Eq. (115):

$$V_{total} \leq -\frac{1}{2}\alpha_d \parallel e_d, \xi_d \parallel^2 - \frac{1}{2}\gamma_1 V_\omega^{1/2} - \gamma_2 V_\omega - \frac{1}{2}\lambda_{min}(Q_{ob}) \parallel e_z \parallel^2 - \beta_c V_c + C \tag{126}$$

Step 6: Large-Signal Stability Theorem of the Closed-Loop System

Theorem 6.5 (Practical Stability of the Overall Closed-Loop System): *Consider the closed-loop system consisting of the PMSM mathematical model (Eqs. (1)–(4)), the d-axis PI controller with anti-windup strategy (Eqs. (92) and (93)), the q-axis enhanced adaptive super-twisting current constraint controller (Eq. (15)), the fourth-order GPIO (Eq. (19)) and the voltage saturation constraint (Eq. (95)). If the following four conditions are satisfied:*

The basic assumptions of the system, i.e., *Assumptions 6.1–6.4, hold;*

The sliding mode control gain is selected to satisfy the constraint condition in Eq. (62):

$$k_1 > \frac{\rho^+}{2}, k_2 > \frac{\rho^+}{4} + \frac{(\rho^+)}{8k_1}$$

The PI control gains are designed to satisfy $k_{pd} > 0$, $k_{id} > 0$ and $k_{pd} > \frac{R_s}{L_s}$;

The observer poles are configured reasonably such that the matrix A_{ob} is a Hurwitz matrix;

There exists a positive constant $\eta > 0$ such that the time derivative of the composite Lyapunov function satisfies the following inequality:

$$\dot{V}_{total} \leq -\eta V_{total}^{1/2} + C \tag{127}$$

where C is proportional to the saturation deviation $\|\Delta u_{sat}\|^2$ (C = 0 when saturation is not activated). Therefore:

When the voltage saturation of the system is not activated (C = 0), the derivative of the composite Lyapunov function is negative definite, and the system states converge exponentially to the origin;

When the voltage saturation of the system is activated transiently (C > 0), the system states are uniformly ultimately bounded, and all state variables converge to the following compact set:

$$\Omega = \left\{ \chi : V_{total} \leq \left(\frac{2C}{\eta}\right)^2 \right\} \tag{128}$$

Proof: Based on the estimation result of the composite Lyapunov function derivative in Eq. (117), the proof is completed by using the following three inequality relationships:

$$\parallel e_d, \xi_d \parallel^2 \geq 2V_d$$

(can be proven by Eq. (97) through appropriate selection of the coupling coefficient)

$$V\omega^{1/2} \geq \lambda_{\min}^{1/2}(P) \parallel \zeta \parallel$$

(derived from the Rayleigh quotient inequality of symmetric matrices)

$$V_c \geq \frac{1}{2}\Phi(i_q)$$

(obtained directly from the definition of the relevant var iables)

There exists a positive constant η_1, η_2, η_3, η_4 such that:

$$\dot{V}_{total} \leq -\eta_1 V_d - \eta_2 V_\omega^{1/2} - \eta_3 V_{ob} - \eta_4 V_c + C \tag{129}$$

From the inequality $\sqrt{a+b} \leq \sqrt{a} + \sqrt{b}$, it follows that:

$$\sqrt{V_{total}} = \sqrt{V_d + V_\omega + V_{ob} + V_c} \leq \sqrt{V_d} + \sqrt{V_\omega} + \sqrt{V_{ob}} + \sqrt{V_c} \tag{130}$$

Moreover, since $\sqrt{V_\omega} \leq \frac{V_\omega^{1/2}}{\lambda_{\min}^{1/4}(P)}$, there exists a constant $\eta > 0$ such that:

$$\dot{V}_{total} \leq -\eta V_{total}^{1/2} + C \tag{131}$$

According to the standard uniform ultimate boundedness theory, when $V_{total} > (2C/\eta)^2$ is $\dot{V}_{total} < 0$, all trajectories eventually enter the compact set Ω. □

Step 7: Explanation of Voltage Saturation Handling

When voltage saturation is activated, C > 0 in Eq. (117) is proportional to the saturation deviation $\|\Delta u_{sat}\|$. The stability of the system is maintained through the following mechanisms:

1. d-axis anti-saturation: The conditional integration strategy (Eq. (93)) halts the integrator during saturation to prevent integral windup and ensure that V_d remains bounded;
2. q-axis robustness: Sliding mode control possesses inherent robustness to input saturation. The control error resulting from saturation can be viewed as a bounded disturbance, which does not compromise the finite-time convergence property of the sliding mode dynamics;
3. Saturation duration: As the current constraint term $k_2\phi\left(i_q\right)s$ increases rapidly when approaching the boundary i_q, it compels the control quantity to revert, resulting in saturation that occurs only briefly during the startup transient.

Therefore, although the system cannot accurately track the desired control quantity when saturation is activated, the state trajectories remain bounded, and the system resumes exponential convergence after exiting saturation.

Conclusion: By constructing a composite Lyapunov function, $V_{total} = V_d + V_\omega + V_{ob} + V_c$ demonstrates the large-signal stability of the PMSM speed control system, which incorporates the d-axis PI integrator, sliding mode control, GPI0, and voltage saturation. The system exhibits exponential convergence to the origin when voltage saturation is inactive, while the system states remain uniformly ultimately bounded during brief activation of saturation.

6.9 Summary

This chapter establishes a comprehensive stability analysis framework for the proposed composite control approach. Through the development of a composite Lyapunov function that encompasses the d-axis PI integral states, sliding mode variables, observer error, and current-constrained barrier function, it is proven rigorously that the q-axis sliding mode subsystem achieves finite-time convergence under the specified gain condition. Moreover, it is shown that the current consistently adheres to the predetermined constraints, and the entire interconnected system, inclusive of the PI controller with voltage saturation, exhibits large-signal stability. The theoretical underpinning provided in this chapter offers robust support for the proposed enhanced adaptive super-helical current-constrained control with a generalized proportional-integral observer composite scheme, thereby ensuring the practical viability and resilience of the system.

7 Simulation Study Analysis

In order to verify the practical effect of the composite control scheme of "enhanced adaptive super-twisting current constraint + generalized proportional-integral observer" (CCEASTA+GPIO) under the non-cascade architecture, we have built a corresponding simulation model in the Matlab/Simulink environment. The specific parameters of the permanent magnet synchronous motor used in the simulation are shown in Table 2.

Table 2: Parameters of table-mounted permanent magnet synchronous motor.

Parameter	Numerical Value
Stator resistance R/Ω	1.74
Winding inductance L/mH	4
Magnetic pole pair number p	4
Permanent magnet chain ψ_F/Wb	0.3
Moment of inertia J/(kg·m^2)	0.000178
Coefficient of viscous friction β (N·m·(rad·s)$^{-1}$)	0
Rating P_N/KW	0.75
Rated voltage U_N/V	220
Rated current I_N/A	4.7
Rated speed n_N/(r/min)	3000
Rated torque T_N(N·m)	2.387

To assess the efficacy of the composite control strategy, it is juxtaposed against two alternative schemes: one employing a composite controller integrating the super-twisting algorithm with the extended state observer (STA+ESO), and the other utilizing a composite approach merging proportional-integral control with the extended state observer (PI+ESO). The composite control system CCEASTA+GPIO is designated as Scheme 1, the STA+ESO composite control system as Scheme 2, and the PI+ESO composite control system as Scheme 3.

To ensure a fair comparison, the parameters of the three control schemes are optimized independently to achieve the best dynamic performance for each scheme. The optimization process for the two comparative schemes is as follows: for the STA+ESO scheme, the current loop gain k_{11}, k_{12} and speed loop gain k_{21}, k_{22} are adjusted using a trial-and-error method, with the objectives of eliminating overshoot in the step response and minimizing regulation time, while also preventing excessive oscillation in the shaft current. The ESO parameters β_{01}, β_{02} are selected based on the bandwidth method and are fine-tuned to balance speed estimation and noise suppression. A similar approach is employed for the PI+ESO scheme, where the speed loop PI parameters k_{41}, k_{42} are initially adjusted according to the Ziegler-Nichols method and then refined, while the current loop PI parameters k_{31}, k_{32} are set to ensure rapid tracking of the shaft current without overshoot. Once all parameters are established, they remain constant throughout the comparison simulation, thereby ensuring a fair evaluation.

The parameter selected for Scheme 1 include $\lambda_1 = 15$, $\lambda_2 = 27$, $k_1 = 230$, $k_2 = 10$, $\alpha = 120$, $\gamma_1 = 4$, $\gamma_2 = 16$, and $\varepsilon = 0.001$. The poles of the generalized proportional-integral observer are configured as $\beta_1 = 120$, $\beta_2 = 5400$, $\beta_3 = 108{,}000$, and $\beta_4 = 81{,}000$. For Scheme 2, the current loop parameters are $k_{11} = 8$ and $k_{12} = 130$, while the velocity loop parameters are k_{21} = 2 and k_{22} = 60. The expanded state observer parameters are β_{01} = 9100, β_{02} = 810, α = 0.5, and δ = 0.01. The parameters selected for Scheme 3 include current loop parameters k_{31} = 10 and k_{32} = 115, velocity loop parameters k_{41} = 1 and k_{42} = 40, and expanded state observer parameters β_{01} = 8410, β_{02} = 810, α = 0.5, and δ = 0.01.

To thoroughly assess the performance of the proposed scheme, the simulation is divided into two segments: one that examines ideal conditions and another that compares simulations conducted under both ideal and non-ideal conditions.

7.1 Simulation under Ideal Conditions

The ideal state simulation presupposes the absence of measurement noise, non-ideal inverter characteristics, calculation delays, and voltage saturation. This section evaluates the performance of three schemes across several dimensions, including no-load starting, load mutation, speed steps, and disturbance suppression.

Fig. 2 shows the speed comparison curve, Fig. 3 shows the q-axis current start-up response curve, and Table 3 shows the response time and overshooting amount data, which shows that Scheme 1 limits the peak current within the limit value, Scheme 2 and Scheme 3 fail to limit the current within the limit value, and Scheme 1 has the optimal start-up speed response.

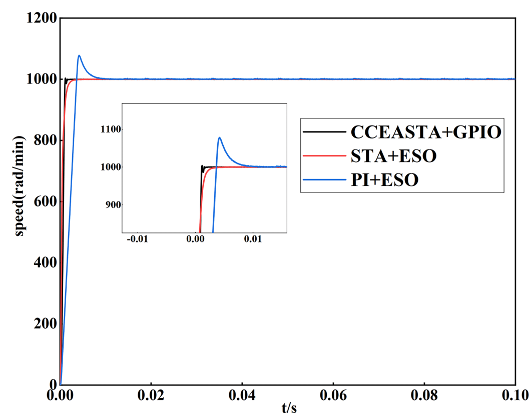

Figure 2: Comparison of motor speed response during no-load starting.

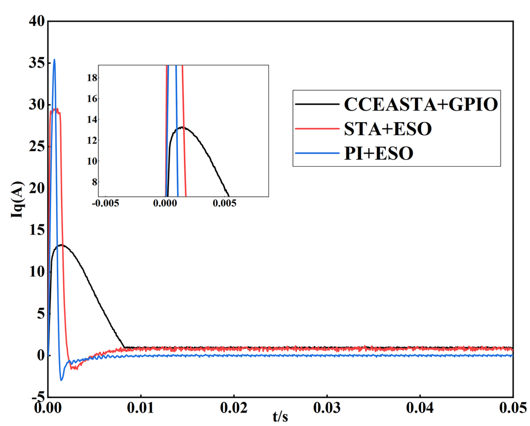

Figure 3: q-axis starting current response curve.

Table 3: Speed performance of PMSM startup phase.

	CCEASTA+GPIO	STA+ESO	PI+ESO
Response time t/s	0.002	0.004	0.008
Overshoot %	0.5	0	7.6

The analysis shows that only Scheme 1 (i.e., the method proposed in this paper) strictly limits the peak q-axis current within the preset constraints. In contrast, both Scheme 2 and Scheme 3 fail to effectively maintain the current below the limit value. In addition, in terms of rotational speed response, Scheme 2 has no overshoot but the regulation time is longer than that of Scheme 1. Scheme 3 has higher overshoot and longer regulation time compared with Schemes 1 and 2. Therefore, Scheme 1 has the best overall dynamic performance.

Figs. 4–6 show the steady state torque curves of the three schemes when a load torque of 5 N·m is applied to the system. Table 4 shows the torque pulsation ranges and torque pulsation ratios of the three schemes, and after comparative analysis, Scheme 1 of the three schemes has a better performance in suppressing torque pulsation.

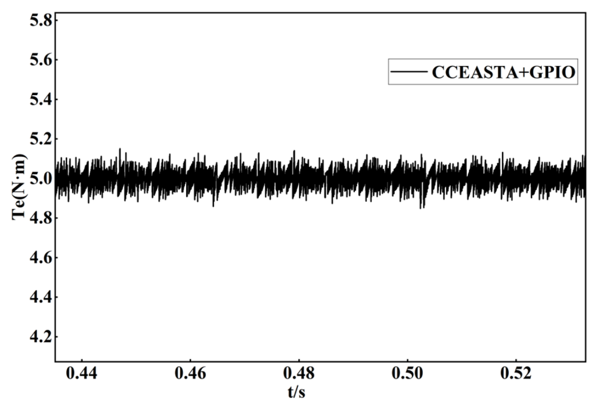

Figure 4: CCEASTA+GPIO steady-state torque curve.

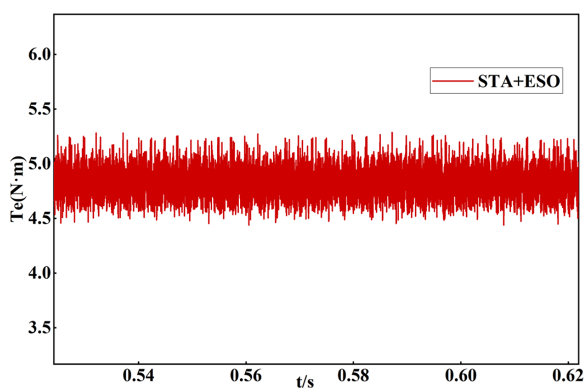

Figure 5: STA+ESO steady-state torque curve.

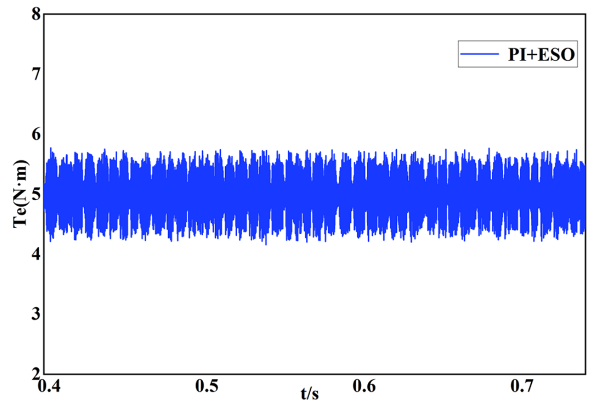

Figure 6: PI+ESO steady-state torque curve.

Table 4: Load torque pulsation data.

	CCEASTA+GPIO	STA+ESO	PI+ESO
Torque ripple range (N·m)	4.9~5.1	4.4~5.3	4.2~5.8
Torque ripple ratio (%)	4	18	32

Comparison of the three schemes in the lift-speed performance, start the given speed of 200 r/min, in 0.02 s will be given to 1000 r/min speed, in 0.06 s will be given to 600 r/min speed. According to Fig. 7, Tables 5 and 6 can be obtained, in the three schemes among the Scheme 2 overshooting amount of 0, but the response time is longer than the Scheme 1, the Scheme 3 compared to the scheme has, the Scheme 2 overshooting is higher, a comprehensive comparison of Scheme 1 can be better performance of lift speed.

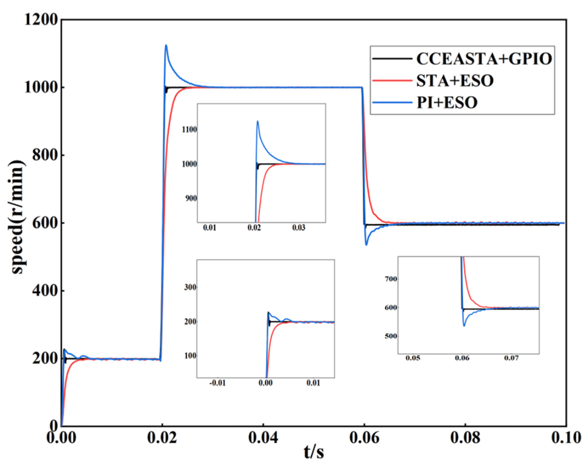

Figure 7: Comparison curve of variable speed response of composite control system.

Table 5: System variable speed response time.

	CCEASTA+GPIO	STA+ESO	PI+ESO
200 r/min(t/s)	0.001	0.005	0.008
1000 r/min(t/s)	0.002	0.004	0.007
600 r/min(t/s)	0.002	0.007	0.006

Table 6: System variable speed response overshoot.

	CCEASTA+GPIO	STA+ESO	PI+ESO
200 r/min(%)	7.5	0	8
1000 r/min(%)	4	0	10.5
600 r/min(%)	3.3	0	11.6

In this study, the immunity performance of the system is tested by two types of disturbances, step and sine wave. For the unknown step disturbance applied at 0.06 s, Fig. 8 shows that Scheme 1(CCEASTA+GPIO) has the fastest response (0.01 s) and the smallest speed fluctuation (18 r/min), while Schemes 2 and 3 have a slower response (0.13 s) and significant fluctuation (87 r/min). In addition, under the amplitude-phase unknown sinusoidal disturbance applied for 0.03 s, Scheme 1 still exhibits the best disturbance suppression and tracking performance as shown in Fig. 9. The results show that the proposed scheme is superior in different disturbance modes.

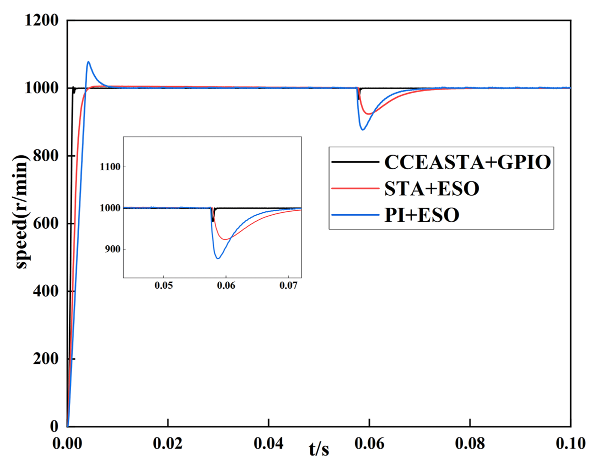

Figure 8: Comparison curves of step disturbance.

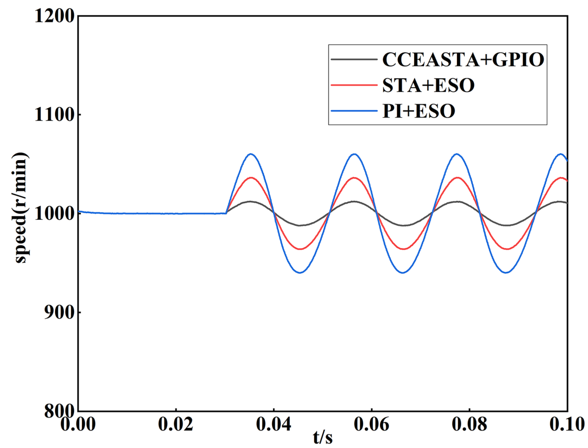

Figure 9: Comparison curve of sine wave disturbance.

7.2 Comparison of Simulations between Ideal and Non-Ideal States

To assess the feasibility and robustness of the proposed CCEASTA+GPIO scheme within a practical digital control environment, this section compares and analyzes both the ideal simulation model and the simulation model incorporating non-ideal factors. These non-ideal factors encompass sensor noise, measurement offset, discretization delay, inverter non-linearity, and voltage saturation. The specific parameter settings are established based on typical device manuals and engineering experience, as detailed in Table 7.

Table 7: Parameter settings of non-ideal factors.

Non-Ideal Factors	Parameter	Value	Basis
Current noise	Root mean square value	0.1 A	Noise level of LEM HAS series sensors
Current offset	Constant offset	0.2 A	Typical value of temperature drift of conditioning circuit
Speed noise	Root mean square value	5 r/min	Quantization noise of 2500-line encoder
Sampling period	Discretization step	100 μs	Corresponding to PWM switching frequency 10 kHz
Computation delay	One-beat delay	1 sampling period	Implementation features of digital signal processor/field programmable gate array (DSP/FPGA)
Dead time	IGBT dead time	2 μs	Typical value of Infineon FS50R06
On-state voltage drop	IGBT voltage drop	1.0 V	Typical value at rated current
Diode voltage drop	Freewheeling voltage drop	1.5 V	Typical value of anti-parallel diode

(Continued)

Table 7 (continued)

Non-Ideal Factors	Parameter	Value	Basis
DC bus voltage	Voltage amplitude	300 V	After rectification corresponding to 220 V AC
Speed filtering	Low-pass cut-off frequency	500 Hz	Engineering empirical value
Current filtering	Low-pass cut-off frequency	1 kHz	Higher than current loop bandwidth

Under ideal and non-ideal conditions, the CCEASTA+GPIO scheme is respectively simulated and tested, and the simulation is shown in Figs. 10–15 below.

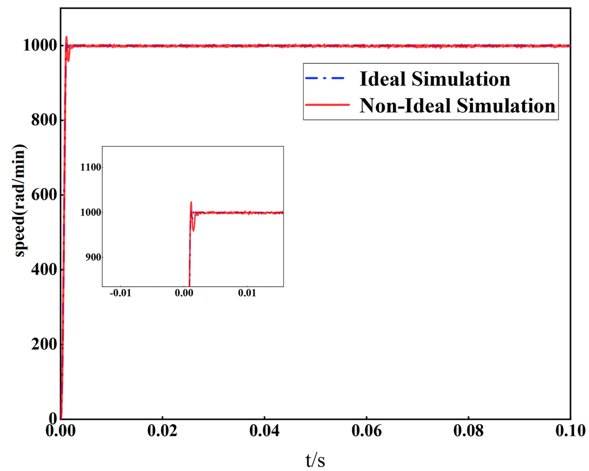

Figure 10: Comparison of starting speeds in ideal and non-ideal states.

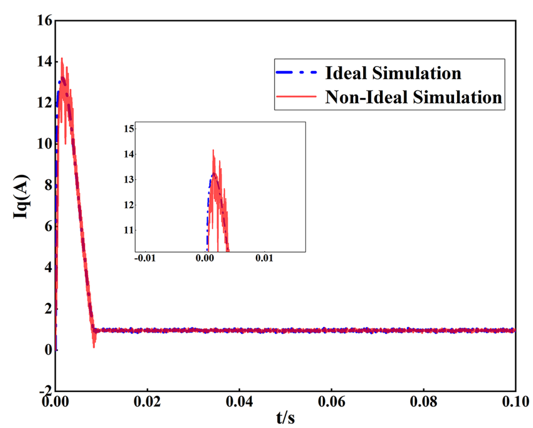

Figure 11: Comparison of starting currents between ideal and non-ideal states.

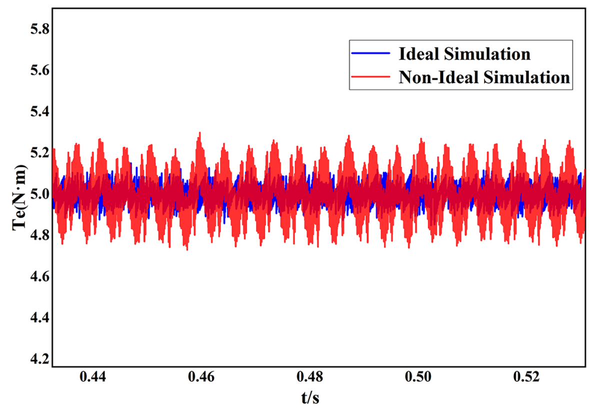

Figure 12: Comparison of steady-state torques between ideal and non-ideal states.

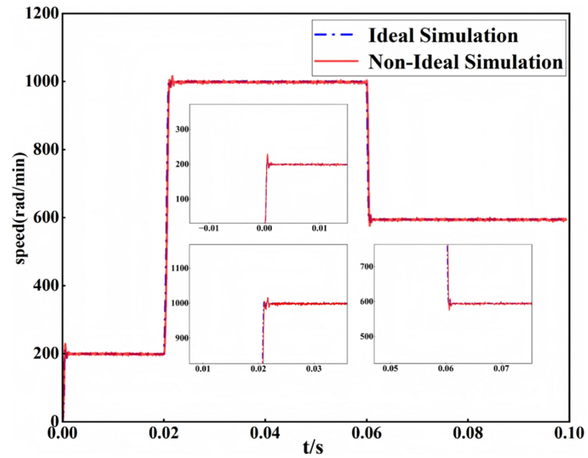

Figure 13: Comparison of variable speed responses between ideal and non-ideal states.

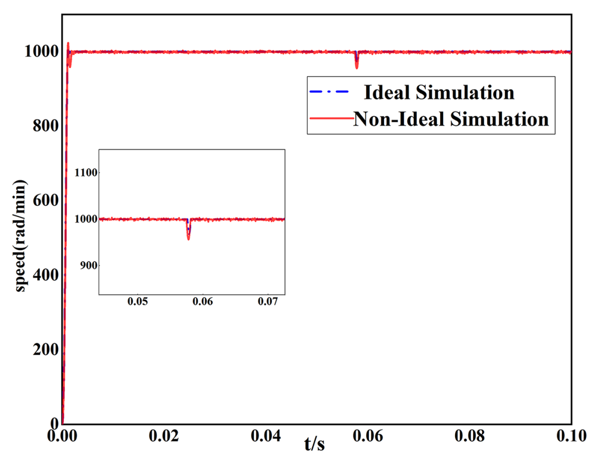

Figure 14: Comparison of load disturbances between ideal and non-ideal states.

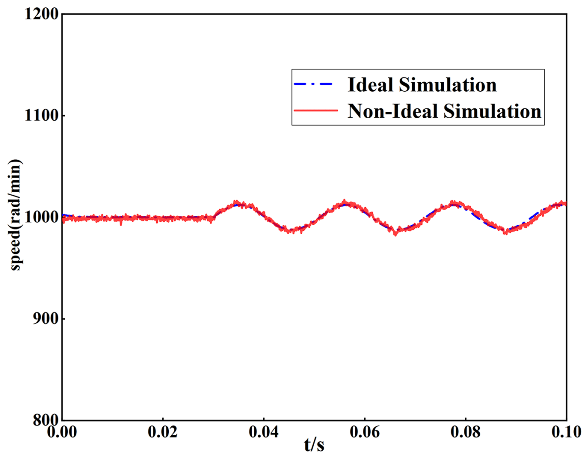

Figure 15: Comparison of sinusoidal disturbance between ideal state and non-ideal state.

Fig. 10 and Table 8 indicate that, under non-ideal conditions, the initial speed response is delayed by 0.0005 s relative to ideal conditions; however, it still effectively tracks the set value. The overshoot increases by 1.8% compared to ideal conditions, yet the overall dynamic performance remains satisfactory, with no observed oscillations or instability.

Table 8: Speed performance of PMSM in the starting stage under two states.

	Ideal-State CCEASTA+GPIO	Non-Ideal-State CCEASTA+GPIO
Response time t/s	0.002	0.0025
Overshoot %	0.5	2.3

Fig. 11 demonstrates that the starting current on the q-axis remains firmly within the predetermined constraint range. Despite minor ripples caused by noise and dead zones, the peak current does not surpass the established limit. This observation indicates that the current constraint mechanism exhibits considerable robustness against non-ideal factors.

Fig. 12 and Table 9 indicate that, following the introduction of non-ideal factors, the steady-state torque ripple experiences a slight increase; however, it remains at a low level. Furthermore, there is no evident high-frequency oscillation or amplitude mutation, suggesting that the system effectively suppresses influences such as sensor noise and inverter nonlinearity.

Table 9: Load torque ripple data in two states.

	Ideal-State CCEASTA+GPIO	Non-Ideal-State CCEASTA+GPIO
Torque ripple range (N·m)	4.9~5.1	4.8~5.2
Torque ripple ratio (%)	4	8

Fig. 13, Tables 10 and 11 demonstrate that, under variable speed conditions, the rotational speed tracking can rapidly respond to changes even in non-ideal circumstances. While there is a slight increase in overshoot and response time, the overall dynamic characteristics remain close to the ideal state. This observation indicates that the control system exhibits strong adaptability to digital implementation errors, including sampling delay and discretization.

Table 10: Variable speed response time of the system in two states.

	Ideal-State CCEASTA+GPIO	Non-Ideal-State CCEASTA+GPIO
200 r/min(t/s)	0.001	0.002
1000 r/min(t/s)	0.002	0.002
600 r/min(t/s)	0.002	0.003

Table 11: Overshoot of the variable speed response of the two-state system.

	Ideal-State CCEASTA+GPIO	Non-Ideal-State CCEASTA+GPIO
200 r/min(%)	7.5	14.5
1000 r/min(%)	0.4	1.6
600 r/min(%)	3.3	4

Fig. 14 and Table 12 illustrate that, in response to sudden load disturbances, the amplitude of speed reduction under non-ideal conditions is marginally greater than that observed in ideal circumstances. However, the recovery time remains largely consistent, with no divergence or sustained oscillation detected. This finding indicates that the integration of the observer and the controller continues to be effective for disturbance estimation and feedforward compensation.

Table 12: Comparison of system step disturbance data between the two states.

	Ideal-State CCEASTA+GPIO	Non-Ideal-State CCEASTA+GPIO
Response time (s)	0.01	0.015
Perturbation change amount (r/min)	18	22

Fig. 15 illustrates that, in the presence of sine disturbances, the amplitude of speed fluctuations under non-ideal conditions increases relative to the ideal state. Nevertheless, the system continues to exhibit robust tracking performance, suggesting that it retains a strong capacity to suppress complex time-varying disturbances.

The comparison and analysis of simulations under both ideal and non-ideal conditions demonstrate that the proposed CCEASTA+GPIO composite control strategy retains excellent dynamic and steady-state performance despite the introduction of real-world non-ideal factors, including sensor noise, measurement offset, discretization delay, inverter nonlinearity, and voltage saturation. Specifically, the system exhibits a rapid response during startup and speed variations without significant oscillation. Additionally, the q-axis current remains strictly confined within the predetermined safety limits, while the steady-state torque ripple is maintained at a low level. Furthermore, the strategy effectively suppresses both step and sine disturbances. These findings indicate that the proposed scheme possesses strong feasibility and robustness within actual digital control environments, highlighting its potential for engineering applications.

8 Conclusion

This paper addresses the issue of overcurrent protection and the need to mitigate both internal and external disturbances in the non-cascade structure of permanent magnet synchronous motors. We propose a composite control strategy that integrates enhanced adaptive super-twisting current constraint control with a generalized proportional integral observer. The enhanced adaptive super-twisting sliding mode control effectively reduces chattering associated with sliding mode control and enhances both dynamic and steady-state performance through the use of a continuously differentiable switching function and a speed-adaptive gain. The current constraint control enforces strict limits on the q-axis current in the non-cascade structure by incorporating a barrier function, thereby preventing hardware damage due to instantaneous overcurrent. Additionally, the generalized proportional integral observer provides real-time estimation and feedforward compensation for the system's lumped disturbances, further improving the system's disturbance rejection capability.

Under optimal simulation conditions, the comparative results of the STA+ESO and PI+ESO schemes indicate that the proposed scheme presented in this paper demonstrates superior dynamic performance in several areas, including startup response, speed change tracking, load mutation, and disturbance suppression. Notably, it effectively confines the q-axis current within the predetermined safety limits while simultaneously significantly reducing the steady-state torque ripple.

On this basis, this paper further introduces practical non-ideal factors such as sensor noise, measurement offset, discretization delay, inverter non-linearity, and voltage saturation in the simulation, and verifies the feasibility and robustness of the proposed scheme in the engineering implementation environment. The simulation results show that the system can still maintain a fast and accurate speed response under non-ideal conditions, the q-axis current always meets the constraint requirements, the torque ripple is controlled at a low level, and it has good suppression ability for step and sinusoidal disturbances. In summary, the proposed composite control strategy in this paper realizes excellent dynamic and steady-state performance on the premise of ensuring the safety and robustness of the system, and provides an effective and feasible solution for high-performance permanent magnet synchronous motor drive systems.

Acknowledgement: The author sincerely expresses gratitude to the professor for his invaluable guidance and support throughout this paper. Appreciation is also extended to the Central Government Guides Local Science and Technology Development Fund for providing financial assistance to this research.

Funding Statement: This research was funded by The Central Guidance on Local Science and Technology Development Fund of Gansu Province, grant number 25ZYJA027. The recipient of the grant is Boqiang Wei.

Author Contributions: The authors confirm contribution to the paper as follows: conceptualization, Yiwei Feng and Boqiang Wei; methodology, Boqiang Wei; software, Boqiang Wei; validation, Boqiang Wei and Yiwei Feng; formal analysis, Boqiang Wei; investigation, Boqiang Wei; resources, Yiwei Feng; data curation, Boqiang Wei; writing—original draft preparation, Boqiang Wei; writing—review and editing, Yiwei Feng and Boqiang Wei; visualization, Boqiang Wei; supervision, Yiwei Feng; project administration, Yiwei Feng; funding acquisition, Yiwei Feng. All authors reviewed and approved the final version of the manuscript.

Availability of Data and Materials: The data that support the findings of this study are available from the corresponding author, Boqiang Wei, upon reasonable request.

Ethics Approval: This study does not involve human or animal subjects, and thus no ethical approval is required.

Conflicts of Interest: The authors declare no conflicts of interest.

Abbreviations

PMSM	Permanent magnet synchronous motor
CCEASTA	Enhanced adaptive super-twisting current-constrained algorithm
GPIO	Generalized proportional-integral observer

References

1. Mehedi F, Yousfi A, Bouyakoub I, Reguieg Z. Advanced control of five-phase PMSM using combined fractional-order super-twisting algorithm with modified SVM approach. J Electr Eng. 2025;76(6):546–56. doi:10.2478/jee-2025-0057.
2. Ismail MM, Al-Dhaifallah M, Rezk H, Refaat MM, Junejo AK. Adaptive linear MPC for a PMSM-driven autonomous EV with a filtered third-order generalized integrator observer. Sci Rep. 2026;16(1):9349. doi:10.1038/s41598-026-39158-3.
3. Lu G, Su J, Yang G, Wang S. Transitional period harmonic current analysis and suppression in dual three-phase PMSMs using generalized integrators. IEEE J Emerg Sel Top Power Electron. 2024;12(4):3862–74. doi:10.1109/JESTPE.2024.3415422.
4. Jiang C, Wang Q, Zhang N, Ding H. Overcurrent protection and unmatched disturbance rejection under non-cascade structure for PMSM. Energies. 2022;15(18):6573. doi:10.3390/en15186573.
5. Preindl M, Bolognani S. Model predictive direct speed control with finite control set of PMSM drive systems. IEEE Trans Power Electron. 2013;28(2):1007–15. doi:10.1109/TPEL.2012.2204277.
6. Kogiso K, Hirata K. Reference governor for constrained systems with time-varying references. In: Proceedings of the 2006 IEEE International Conference on Multisensor Fusion and Integration for Intelligent Systems; 2006 Sep 3–6; Heidelberg, Germany. p. 359–64. doi:10.1109/MFI.2006.265603.
7. Wu M, Yan G, Lin Z, Liu M. Characterization of backward reachable set and positive invariant set in polytopes. In: Proceedings of the 2009 American Control Conference; 2009 Jun 10–12. St. Louis, MO, USA. p. 4351–6. doi:10.1109/ACC.2009.5159817.
8. Wang Y, Shi S, Mai S. Composite high order super-twisting sliding mode control algorithm for PMSMs based on dung beetle optimization. J Power Electron. 2025;25(7):1198–207. doi:10.1007/s43236-024-00969-0.
9. Zhang Z, Yang X, Wang W, Chen K, Cheung NC, Pan J. Enhanced sliding mode control for PMSM speed drive systems using a novel adaptive sliding mode reaching law based on exponential function. IEEE Trans Ind Electron. 2024;71(10):11978–88. doi:10.1109/TIE.2023.3347845.
10. An J, Zhang Z, Pan J. Sensorless control of permanent magnet synchronous motor based on adaptive sliding mode observer and phase locked loop. In: Proceedings of the 10th International Conference on Power Electronics Systems and Applications (PESA); 2024 Jun 5–9; Hong Kong, China. p. 1–4. doi:10.1109/PESA62148.2024.10595026.
11. Zhang J, Ren W, Sun XM. Extended-state-observer-based nonlinear control for PMSM servo systems with current constraints and voltage saturations. IEEE Trans Transp Electrif. 2024;10(2):2713–26. doi:10.1109/TTE.2023.3304173.
12. Shah AP, Mehta AJ. Direct power control of DFIG using super-twisting algorithm based on second-order sliding mode control. In: Proceedings of the 2016 14th International Workshop on Variable Structure Systems (VSS); 2016 Jun 1–4; Nanjing, China. p. 136–41. doi:10.1109/VSS.2016.7506905.
13. Hu J, Lu H, Zheng B, Zhang Y. Predictive control of permanent magnet synchronous motor based on Super-Twisting sliding mode. Energy Sci Eng. 2023;11(9):3173–84. doi:10.1002/ese3.1512.
14. Yao G, Cheng Y, Wang Z, Xiao Y. Study on a second-order adaptive sliding-mode observer control algorithm for the sensorless permanent magnet synchronous motor. Processes. 2023;11(6):1636. doi:10.3390/pr11061636.
15. Dou W, Ding S, Park JH, Mei K. An adaptive generalized super-twisting algorithm via event-triggered control. IEEE Trans Autom Sci Eng. 2025;22:393–406. doi:10.1109/TASE.2024.3351122.
16. Song YS, Zhuo SQ, Li FS, Wang X, Guo CX, Shen CW. Control strategy of permanent magnet synchronous motor based on enhanced adaptive super-twisting sliding mode observer. Electr Mach Control. 2025;29(6):1–11. (In Chinese).

17. Hou Q, Ding S. GPIO based super-twisting sliding mode control for PMSM. IEEE Trans Circuits Syst II Express Briefs. 2021;68(2):747–51. doi:10.1109/TCSII.2020.3008188.
18. Su J, Chen WH, Yang J. On relationship between time-domain and frequency-domain disturbance observers and its applications. J Dyn Syst Meas Control. 2016;138(9):091013. doi:10.1115/1.4033631.
19. Zhang B, Wei B. A STA current-constrained control for PMSM speed regulation system with function disturbance observer. Energy Eng. 2022;119(3):1197–218. doi:10.32604/ee.2022.018411.
20. Le TL, Hsieh MF. A combined control method for permanent magnet synchronous motor drives with sliding mode control and observer approach. Comput Electr Eng. 2026;129(4):110812. doi:10.1016/j.compeleceng.2025.110812.
21. Ismail MM, Xu W, Ge J, Tang Y, Junejo AK, Hussien MG. Adaptive linear predictive model of an improved predictive control of permanent magnet synchronous motor over different speed regions. IEEE Trans Power Electron. 2022;37(12):15338–55. doi:10.1109/TPEL.2022.3194839.
22. Jia L, Lin M, Le W, Li N, Kong Y. Dual-skew magnet for cogging torque minimization of axial flux PMSM with segmented Stator. IEEE Trans Magn. 2020;56(2):7507306. doi:10.1109/TMAG.2019.2951704.